



1 **Geothermal heat flow in Antarctica: current and future**
2 **directions**

3 Alex Burton-Johnson¹, Ricarda Dziadek², and Carlos Martin¹

4 ¹British Antarctic Survey, High Cross, Madingley Road, Cambridge, CB3 0ET, UK

5 ²Alfred Wegener Institute - Helmholtz Centre for Polar and Marine Research, Am Alten Hafen, Bremerhaven,
6 Germany

7 *Correspondence to:* Alex Burton-Johnson (alerto@bas.ac.uk)

8 **1. Abstract**

9 Antarctic geothermal heat flow (GHF) affects the temperature of the ice sheet, determining its ability to slide and
10 internally deform, as well as the behaviour of the continental crust. However, GHF remains poorly constrained,
11 with few and sparse local, borehole-derived estimates, and large discrepancies in the magnitude and distribution
12 of existing continent-scale estimates from geophysical models. We review the methods to extract GHF, compile
13 borehole and probe-derived estimates from measured temperature profiles, and recommend the following future
14 directions: 1) Obtain more borehole-derived estimates from the subglacial bedrock and englacial temperature
15 profiles. 2) Estimate GHF beneath the interior of the East Antarctic Ice Sheet (the region most sensitive to GHF
16 variation) via long-wavelength microwave emissivity. 3) Estimate GHF from inverse glaciological modelling,
17 constrained by evidence for basal melting. 4) Revise geophysically-derived GHF estimates using a combination
18 of Curie depth, seismic, and thermal isostasy models. 5) Integrate in these geophysical approaches a more accurate
19 model of the structure and distribution of heat production elements within the crust, and considering
20 heterogeneities in the underlying mantle. And 6) continue international interdisciplinary communication and data
21 access.

22



23 1. Introduction

24 The Antarctic ice sheet is the world's largest potential driver of sea level rise, and accurately modelling its
25 dynamics relies, amongst others, on constraining conditions at the ice-bedrock interface. Measuring these basal
26 conditions is inherently challenging and, of all the parameters affecting ice sheet dynamics, subglacial geothermal
27 heat flow (GHF) is the least constrained (Larour et al., 2012; Llubes et al., 2006). Despite this uncertainty, GHF
28 affects (1) ice temperature and, as a consequence, ice mechanical properties (rheology), (2) basal melting and
29 sliding, and (3) the development of unconsolidated water-saturated sediments; all of which can promote ice flow
30 (Greve and Hutter, 1995; Larour et al., 2012; Siegert, 2000; Winsborrow et al., 2010). Beyond ice dynamics, our
31 knowledge of GHF allows us to model past basal melt rates in our exploration for old ice core climate records,
32 constrain models of glacial isostatic adjustment (GIA), and inform on the geological and tectonic development of
33 Antarctica.

34 In recognition of the ambiguity and importance of Antarctic GHF, an increasing number of studies in geology,
35 geophysics, and glaciology have sought to constrain this parameter, with a developing dedicated multinational
36 interdisciplinary community (Burton-Johnson et al., 2019; Halpin and Reading, 2018). However, with an
37 expanding research base and a requirement for multidisciplinary science, the necessity for a multidisciplinary
38 review of current approaches and future directions was highlighted by the GHF sub-group of SERCE (Solid Earth
39 Response and influence on Cryospheric Evolution) and the Scientific Committee on Antarctic Research (SCAR)
40 (Burton-Johnson et al., 2019).

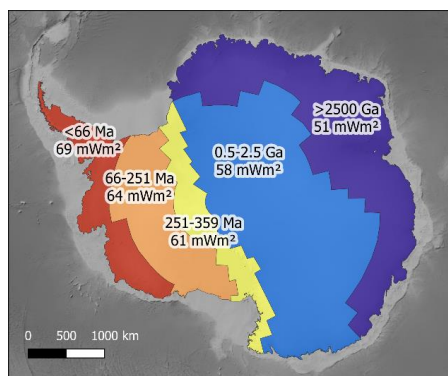
41 1.1. What is geothermal heat flow (GHF)?

42 GHF describes the transport of heat energy from the interior of the Earth to the surface (Gutenberg, 1959; Pollack
43 et al., 1993). This heat originates from two primary sources: 1) The primordial heat remaining from the formation
44 of the Earth, when the kinetic energy of celestial collisions was transformed into heat energy; and 2) the
45 radioactive decay of heat-producing elements (HPEs) and their isotopes; 98% of which is derived from Uranium,
46 Thorium, and Potassium (Beardmore and Cull, 2001; Lowrie, 2007). The HPEs are incompatible with the mineral
47 structures of the mantle, so are concentrated into the crust (Boden, 2016; McDonough and Sun, 1995). Other
48 sources of possible contributions to GHF are: 1) geoneutrino emission from the mantle (Huang et al., 2013;
49 Korenaga, 2011), and 2) gravitational pressure (Elbeze, 2013; Morgan et al., 2016).

50 The estimated average heat flow of continental crust is 67.1 mW m^{-2} , whilst for oceanic crust it is 78.8 mW m^{-2}
51 (Lucazeau, 2019; although estimates vary according to sampling strategy and the number of observations). The
52 difference between continental and oceanic heat flow reflects the lower thickness of oceanic crust, with hot mantle
53 rocks at comparatively shallow depths. Continental GHF varies significantly, primarily in response to variations
54 in crustal heat production, age, composition, tectonic history, and thickness of crust and mantle (Mareschal and
55 Jaupart, 2013). This results from the geological complexity of composite continental crust compared with oceanic
56 crust. GHF is generally lower in stable crust away from convergent and divergent continental margins and rift
57 basins, and higher in these magmatically active provinces (Lucazeau, 2019; Pollack et al., 1993). On a broad
58 regional scale, continental GHF correlates negatively with age, allowing first order empirical estimation of
59 Antarctic GHF based on its range of crustal ages (Fig. 1; Llubes et al., 2006; Sclater et al., 1980). However,
60 Antarctic crustal heat production estimates show high variability across sampled age ranges (Gard et al., 2019),



61 with lithology and tectonic setting being important controls on the heat production distribution (Carson et al.,
62 2014; Halpin et al., 2019).



63
64 **Fig. 1. Empirical estimation of GHF based on generalised Antarctic crustal ages and mean global GHF values of**
65 **continental crust of similar age (adapted from Llubes et al., 2006). Basemap bathymetry from ETOPO1 (Amante and**
66 **Eakins, 2009).**

67 The rate of heat flow, Q , can be approximated by the Fourier's Law (Baron Fourier, 1822). In the simple model
68 of a homogenous material with a constant thermal gradient, this equates to:

$$Q = -\kappa \frac{\partial T}{\partial z}$$

69
70 (1)

71 Where Q has the units mW m^{-2} (i.e. power per unit area); T is the temperature (K), z is the vertical distance (m);
72 and κ is the thermal conductivity of the material ($\text{mW m}^{-1} \text{K}^{-1}$). When considering the basal conditions of the
73 Antarctic ice sheet, we are interested in the heat flow at bedrock surface. We also need to consider internal heat
74 production, A ($\mu\text{W m}^{-3}$). For a simple case of constant thermal conductivity and heat production, surface heat flow
75 can be described by:

$$Q = \lambda_d$$

76
77 (2)

78 Where the integral is measured from the surface to a depth, d (Beardsmore and Cull, 2001).

79 We would like to highlight here that most methods to estimate GHF derive it from the temperature gradient, as in
80 Equations 1 and 2. However, these equations are a simplification, as temperature variation over time, surface
81 topography, internal heat production, and variation in the properties of the material all affect the observed
82 temperature gradient.



83 **2. Motivation: What is the importance of GHF in Antarctica?**

84 **2.1. Glaciology**

85 GHF strongly influences the ice sheet temperature. As a consequence, it is a key contributor to basal meltwater
86 production, ice rheology, basal friction, sliding velocity, and erosion (Fahnestock et al., 2001; Goelzer et al., 2017;
87 Hughes, 2009).

88 The heat budget at the base of an ice sheet can be described (Vieli et al., 2018):

89
$$Q_g + Q_s + Q_w + Q_p + Q_f + Q_c = 0$$

90 (3)

91 Where Q_g is the GHF, Q_s is the heat generated by sliding, Q_w is the heat generated by subglacial water flow, Q_p
92 is the heat required to maintain the flowing water at pressure melting point, and Q_f is the heat released by freezing
93 or used by melting; and Q_c is the heat conducted away in the ice towards the ice surface. Of the positive
94 contributions to basal heat, that generated by sliding (Q_s) can be orders of magnitude greater than that from GHF
95 (Q_g), but in slow flowing areas Q_s is negligible and GHF plays a key role in the heat budget (Larour et al., 2012;
96 Pittard et al., 2016a).

97 To illustrate this point, Llubes et al. (2006) modelled a 20 mW m^{-2} increase in GHF across the Antarctic continent
98 (from uniform values of 40 to 60 mW m^{-2}). This resulted in a 6°C increase in the mean basal temperature, from -
99 7°C to -13°C . This variation directly affects the basal melt rates, with a uniform 40 mW m^{-2} generating 6.7 km^3
100 yr^{-1} of basal melting across Antarctica, whilst 60 mW m^{-2} would generate $18 \text{ km}^3 \text{ yr}^{-1}$. However, unlike the GHF
101 values used, the resultant basal temperature variation is non- uniform: Whilst the two heat flow models produce
102 only a few $^\circ\text{C}$ difference in basal temperature near the coast, they generate up to 15°C difference in central East
103 Antarctica. This is because horizontal advection and frictional basal heating are negligible beneath the thick, slow
104 moving ice of East Antarctica, and surface temperatures have a reduced effect on basal conditions (Llubes et al.,
105 2006; Pollard et al., 2005). Also, in these regions of thick ice, the increased pressure brings the basal ice
106 temperature closer to its pressure melting point (PMP; Pollard et al., 2005). Variation in GHF thus determines
107 whether basal melting occurs, with a resultant effect on the basal friction and sliding of the ice sheet (Pollard et
108 al., 2005). In addition, the increased ice temperature makes it more susceptible to internal deformation, which also
109 enhances its ability to flow (Llubes et al., 2006).

110 Even beneath the comparatively thinner ice of West Antarctica, the sensitivity of basal temperature to heat flow
111 is enhanced (Llubes et al., 2006). There is evidence that this region, dominated tectonically by the West Antarctic
112 Rift System (Jordan et al., 2020), exhibits very high values of basal heat flow and resultant basal melting
113 (Schroeder et al., 2014). Above 85 mW m^{-2} , the basal temperature of much of the West Antarctic Ice Sheet will
114 pass its pressure melting point (in agreement with radar evidence for extensive basal melting; Llubes et al., 2006;
115 Rémy and Legresy, 2004; Schroeder et al., 2014). Consequently, enhanced basal heat flow in West Antarctica can
116 have a large effect on its basal melt rates, although the thinner ice sheet in West Antarctica compared to East
117 Antarctica makes it more sensitive to surface parameters (accumulation and surface temperature; Llubes et al.,
118 2006).



119 In addition to enhancing basal melting and reducing basal friction, increased GHF enhances ice flow by increasing
120 the englacial temperature and thus reducing the ice stiffness (Larour et al., 2012). Because the heat produced by
121 basal friction and viscous deformation are orders of magnitude greater than from GHF in fast-flowing ice streams,
122 this effect is only significant in upstream, slow-flowing areas (Larour et al., 2012). In these regions of thick, slow-
123 flowing ice, even local high heat flow anomalies of insufficient heat for basal melting can result in the
124 development of accelerated, channelised flow for hundreds of kilometres upstream and downstream of the GHF
125 anomaly (Pittard et al., 2016a). Regions along ice divides and adjacent to ice streams are particularly sensitive to
126 enhanced GHF (Pittard et al., 2016b).

127 Whilst the points above highlight the necessity of estimating Antarctic GHF, it is very important that the accuracy
128 of these estimates can be verified. The impact of inaccurate GHF constraints on models of ice sheet dynamics
129 have been shown by comparing GHF estimates for Greenland. Ice sheet modelling controlled by spatially variable
130 GHF forcing reproduces the observed state to only a limited degree, and fails to reproduce either the topography
131 or the low basal temperatures measured in southern Greenland (Rogozhina et al., 2012). Instead, an unrealistic
132 spatially uniform GHF forcing produces a considerably better fit. If the much larger Antarctic ice sheet is to be
133 accurately modelled, the accuracy of the GHF estimates used must be well constrained by multiple independent
134 methodologies, sensitivity tests, and comparison of different models.

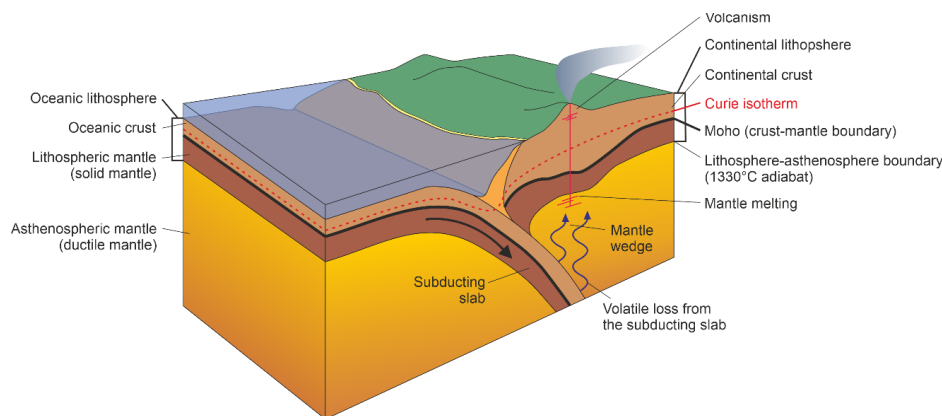
135 Recently, there has been increasing interest in the exploration of suitable locations for coring Antarctica's oldest
136 continuous ice record. This problem requires accurate knowledge of GHF, as basal melt rates limit the maximum
137 possible age of recoverable ice (Liefvering et al., 2018). Additionally, due to environmental concerns around
138 possible drilling fluid contamination, frozen bed conditions are a prerequisite for deep coring operations.

139 2.2. Glacial Isostatic Adjustment (GIA)

140 The temperature of the lithosphere and upper mantle are important parameters for modelling the isostatic response
141 to changes in the volume of the overlying ice sheet (i.e. glacial isostatic adjustment, GIA). This is because the
142 (visco-)elastic properties of the lithosphere and mantle directly relate to its thermal properties (Chen et al., 2018;
143 Kuchar and Milne, 2015). GIA is a critical component of the long-term evolution of ice sheets and could
144 potentially stabilise retreating ice streams in submarine settings (Barletta et al., 2018; Kingslake et al., 2018). Of
145 particular importance here is that the temperature-dependant viscosity that controls GIA can be modelled using
146 surface heat flow estimates (van der Wal et al., 2013, 2015).



147 **2.3. Geology and tectonics**



148

149 **Fig. 2. Basic illustration of a subduction zone at a convergent margin between oceanic and continental lithosphere to**
150 **clarify the geological concepts and terms used in this paper.**

151 **2.3.1. Mantle dynamics**

152 Heat flow variation and its isostatic effects (i.e. the buoyancy control on crustal elevation, resulting from the
153 different densities of the dense mantle and less dense overlying crust) provide evidence for mantle dynamics
154 beneath a continent. For example, high heat flow anomalies have been proposed as evidence for sub-lithospheric
155 heating by present and past mantle plumes (regional hot spots of warm mantle upwelling beneath the lithosphere;
156 e.g. Courtney and White, 1986; Martos et al., 2018), and the absence of enhanced heat flow where mantle ascent
157 is proposed has been used to argue against such processes (e.g. Stein and Stein, 2003). Also, because of the
158 relationship between surface heat flow and isostatic elevation, heat flow studies can reveal thermal or
159 compositional variation of the sub-continental mantle, as a reduction in its density can increase the isostatic
160 elevation of the surface topography (Hasterok and Gard, 2016).

161 **2.3.2. Development of the lithosphere**

162 The thermal properties of the lithosphere control its response to tectonic deformation (e.g. Sandiford and Hand,
163 1998), such as the development of crustal shear zones and earthquakes. The lithosphere's thermal properties also
164 affect the relative density of lithosphere and underlying mantle, and (as a result of this buoyancy effect) the
165 isostatic surface elevation. This in turn influences the heights of Antarctica's mountain ranges and the depths of
166 its sedimentary basins (McKenzie et al., 2005). For these reasons, understanding the continent's GHF will inform
167 on the development of many of Antarctica's largest tectonic features. For example, the lithospheric extension of
168 the West Antarctic Rift System, the prominent elevation of the Transantarctic Mountains, the deep topographic
169 depression of the Wilkes subglacial basin, and the extensive Palmer Land Shear Zone of the Antarctic Peninsula.

170 **3. GHF estimates from measured temperature gradients**

171 Having highlighted the importance of constraining Antarctica's GHF, the following sections discuss current
172 approaches to its estimation.



173 Local heat flow estimates can be derived by measuring the temperature at various depths below the surface (either
174 in the bedrock, overlying sediments, or within the ice sheet) and deriving a temperature gradient. In Antarctica,
175 GHF has been derived through temperature measurements from boreholes into the bedrock or into the ice sheet,
176 and also from probes into unconsolidated sediments. It is important to recognise that these are “estimates” not
177 “measurements” of GHF, particularly when using them to verify the accuracy of geophysical or inverse GHF
178 estimates. This is because the measured thermal gradient can be affected by processes other than geothermal heat
179 flow, including surface temperature variation and hydrothermal circulation. When evaluating a specific local
180 estimate, its derivation, local geology, and other regional GHF estimates must be considered. Thermal gradients
181 and surface heat flow may vary significantly over 10 km lateral spatial resolutions (Carson et al., 2014) with
182 variations in geology (affecting heat production and conductivity; Carson et al., 2014; Hasterok and Chapman,
183 2011), hydrothermal circulation (affecting local heat convection and redistribution; Fisher and Harris, 2010), and
184 topography (affecting heat diffusion pathways to the surface; Bullard, 1938; Lees, 1910).

185 3.1. Boreholes into bedrock

186 The thermal gradient can be determined by measuring the temperature variation at different depths in the crust.
187 Away from Antarctica, these measurements are from boreholes (commonly those drilled for mineral or
188 hydrocarbon exploration), mineshafts, caves, or other cavities. The temperature gradient of the crust’s uppermost
189 10-50 m is dominantly affected by downward conduction of the surface temperature rather than GHF. To address
190 this, temperature measurements are made over the largest depth range possible (typically 100-1000 m).

191 Borehole temperature measurements are made using wire-line temperature probes, with a thermistor at the leading
192 tip and measurements made progressively downwards to minimise disturbance of the borehole fluids prior to
193 temperature measurement. The temperature is measured from the bore fluid, not the surrounding rock, so an
194 important consideration is the need for thermal equilibration of the wall rock and the borehole fluids following
195 drilling and prior to measurement. In addition, the heat produced during drilling needs to be dissipated from the
196 borehole. As a guide, 10-20 times the drilling time is required before a borehole is equilibrated to within
197 instrument accuracy (Bullard, 1947; Jaeger, 1956), although observations show that after 3 times the drilling time,
198 borehole fluids are within 0.05°C of equilibrium values (Lachenbruch and Brewer, 1959). For the low water flows
199 used in small-core (<4 cm diameter) diamond drilling (compared with wider core diameter rotary drilling)
200 measurements can be taken about two days after drilling cessation, except from the upper and lowermost ~20 %
201 of the borehole (Jaeger, 1961, 1965). As an example, drilling of the multiple Cape Roberts Project boreholes
202 averaged 16-31 m day⁻¹ (Talalay and Pyne, 2017).

203 Depth below the bedrock surface must be considered when taking borehole temperature measurements. Where
204 terrestrial bedrock is exposed, atmospheric temperature and seasonal variation perturbs the thermal gradient in the
205 upper >100 m of the crust. In Antarctica, temperatures from Hole 3 of the Dry Valley Drilling Project provided
206 estimates of “equilibrium” gradient only when deeper than 90 m (Decker, 1974; Decker et al., 1975; Pruss et al.,
207 1974). It may be possible to compensate for seasonal variation in shallower boreholes using long-term
208 observations of the temperature gradient (>1 year), although the previous attempt (from a 7.6 m borehole at
209 McMurdo Station; Risk and Hochstein, 1974) derived an anomalously high GHF estimate (164 mW m⁻², compared
210 to 66 mW m⁻² from a 260 m deep borehole; Decker and Bucher, 1982).

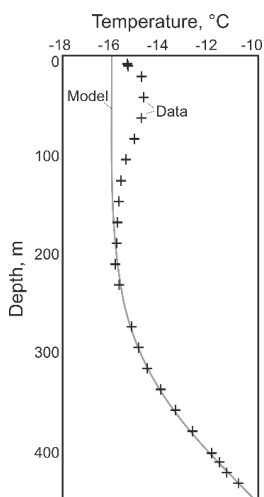


211 Subglacial bedrock is not exposed to atmospheric temperature variation, so the geothermal gradient can be
212 measured from shallower depths. However, it is affected by heat derived from the overlying ice sheet: internal
213 and basal frictional shear heating from the ice sheet, heat advection, basal water, and seasonal temperature
214 variation (e.g. Ritz, 1987). In the absence of a deep, borehole-derived, subglacial bedrock temperature profile, the
215 depth required to accurately measure the unperturbed geothermal temperature gradient is currently unknown.
216 Thermal diffusion modelling over timescales of low frequency climate variation may constrain this.

217 3.2. Ice boreholes

218 Subglacial GHF can be estimated from the temperature gradient from boreholes into the ice sheet (e.g. Engelhardt,
219 2004; Fudge et al., 2019; Nicholls and Paren, 1993). This requires that there is no additional heating from basal
220 shear or horizontal advection, and that ice sheet has been unequivocally frozen to the bed for long enough that the
221 bedrock and overlying ice sheet have thermally equilibrated. To meet this requirement, the temperature profile is
222 best measured from cores into the summits of ice domes where the ice sheet is stationary (Engelhardt, 2004). As
223 applies to bedrock boreholes, a delay between drilling and temperature measurement is required for the thermal
224 disturbance from the drilling to dissipate. For hot-water drilling, this can take 2 years (Barrett et al., 2009;
225 Engelhardt, 2004). The temperature profile is typically measured using thermistors, recording the temperature
226 through changes in resistivity to electrical currents. Either a string of thermistors is deployed into the borehole
227 prior to freezing, and the temperature recorded over time, or the hole can be kept open with drill fluid and
228 downhole temperature measured with a moving thermistor. More recently, temperature has been recorded also
229 using distributed temperature systems (DTS). The temperature is derived from the travel time of a laser beam
230 within an optical fibre. All of these methods require thermal equilibration.

231 Once the englacial temperature profile is obtained, GHF estimation can be achieved through three methods.
232 Firstly, if the borehole reaches the ice-bedrock interface, and the bedrock and overlying ice are in thermal
233 equilibrium, then the GHF can be estimated in the same way as for bedrock boreholes (e.g. Engelhardt, 2004).
234 That is, using the temperature gradient in the ice near the ice-bedrock interface but using the thermal conductivity
235 of ice rather than rock (Equation 1). Secondly, rather than measuring a temperature profile above the bed, the
236 basal temperature at the ice-bedrock interface can be measured, and temperature modelled through time to
237 constrain the required GHF (e.g. Fudge et al., 2019). Thirdly, if the borehole doesn't reach bedrock, and similarly
238 to the previous method, a thermal model is required to constrain GHF (e.g. Zagorodnov et al., 2012). In the
239 methods where modelling is required, the variables are modified within constraints determined for the location
240 until the modelled temperature profile best fits the measurements (Fig. 3), and the modelled temperature gradient
241 within the bedrock used for GHF calculation.



242

243 **Fig. 3. An example of temperature measurements (crosses) and steady state model (grey line) from which GHF can be**
 244 **estimated. Adapted from Zagorodnov et al. (2012) for the LARISSA Site Beta ice borehole temperature profile from**
 245 **the Bruce Plateau, Antarctic Peninsula. Note that it is the deeper temperature gradient that is modelled rather than**
 246 **the shallower temperature variation.**

247 GHF can be estimated from boreholes that do not reach the bedrock providing that the temperature profile is
 248 obtained below the penetration depth (or skin depth, δ) of surface temperature variation into the ice sheet. This
 249 depth is defined by the circular frequency of the variation (ω), and the thermal diffusivity of the material (k)
 250 according to the Equation 4 (Fig. 4; Carslaw and Jaeger, 1959; Wangen, 2010).

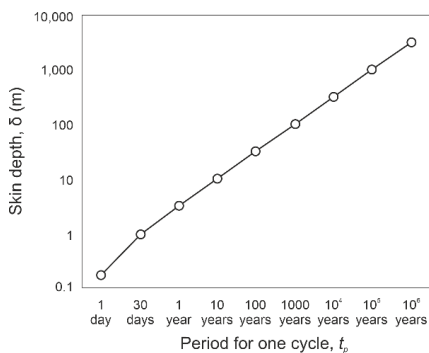
251
$$\delta = \sqrt{(2k/\omega)}$$

252 (4)

253 Where circular frequency (ω) is defined by Equation 5, where t_p is the time for one period (or cycle) of the
 254 temperature variation (Wangen, 2010).

255
$$\omega = 2\pi/t_p$$

256 (5)



257



258 **Fig. 4. Relationship between skin depth and periodicity of temperature variation through a material of thermal**
259 **diffusivity, k , of $10^{-6} \text{ m}^2 \text{ s}^{-1}$. This diffusivity is comparable to ice at -10°C (James, 1968), or average values of a range**
260 **of rock types at -50°C (Vosteen and Schellschmidt, 2003), and increases with decreasing temperature for both**
261 **materials.**

262 The deepest significant perturbations of the englacial temperature profile are from glacial-interglacial cycles, and
263 GHF is best estimated from the englacial temperature profile below the depth at which this effect becomes
264 negligible. In Greenland, this is the bottom 20 % of the ice sheet, but in areas of low-accumulation in Antarctica
265 this can extend to much shallower depths. With sufficiently accurate temperature measurements, the full
266 temperature profile of the ice sheet and the subglacial GHF may be estimated from boreholes penetrating only the
267 upper 600 m or 20 % of the total ice sheet thickness (Hindmarsh and Ritz, 2012; Mulvaney et al., 2019; Rix et al.,
268 2019).

269 However, poorly-constrained thermal effects within the ice sheet propagate uncertainties in GHF estimates from
270 ice sheet boreholes (Cuffey and Paterson, 2010, Chapter 9). This is a particular problem if there is any ambiguity
271 as to whether the ice sheet is frozen to the bed. The englacial temperature profile depends on heat sources at the
272 surface, base, and within the ice (i.e. internal deformation-derived frictional heating). Heat sources that act at the
273 base of the ice, such as frictional heating by basal motion, are impossible to differentiate from GHF.

274 3.3. Marine and onshore unconsolidated sediments

275 Shallow ($< \sim 10 \text{ m}$) temperature gradients in unconsolidated sediments can be recorded using gravity-driven probes
276 rather than drilled boreholes. They carry multiple thermistors along the length of the probe that provide a
277 temperature profile. These measurements can be taken from unconsolidated sediments offshore (e.g. Dziadek et
278 al., 2019, 2017), in subglacial lakes (Fisher et al., 2015) or below ice shelves (Begeman et al., 2017).

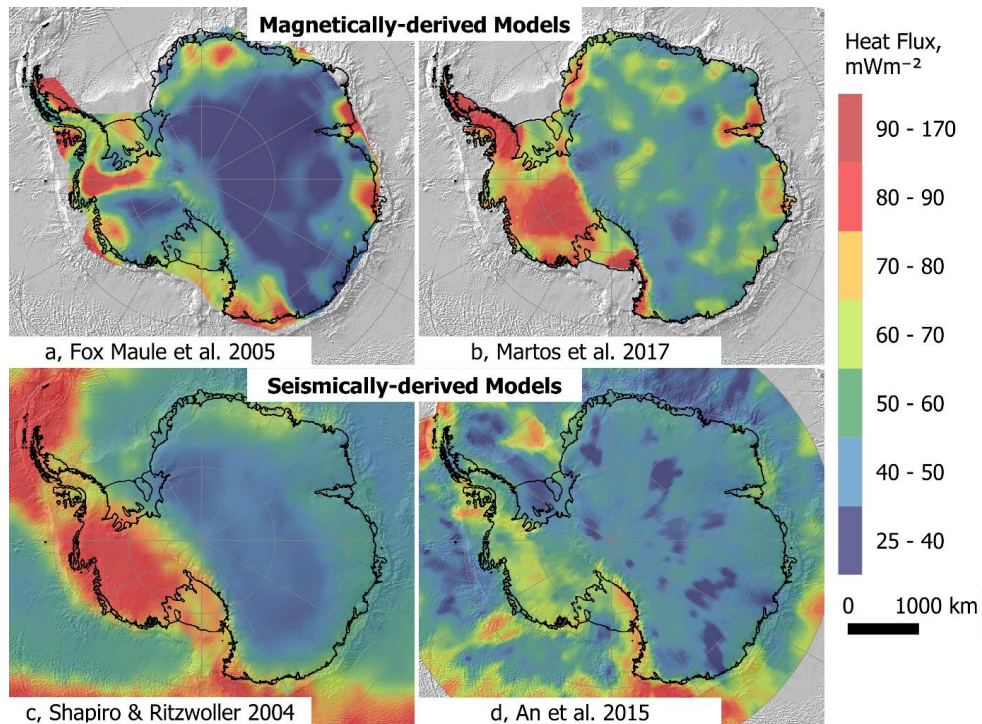
279 As applies to borehole measurements, temperature gradients in unconsolidated sediments must be taken at
280 sufficient depth to represent the crustal temperature gradient and not be perturbed by temperature variation in the
281 overlying water or ice (i.e. they must be representative of steady-state conditions). The penetration depth of
282 temperature variation is dependent on its frequency (Equation 4 and Fig. 4; Carslaw and Jaeger, 1959).
283 Consequently, diurnal or annual cycles only affect the upper few centimetres to couple of metres of the surface
284 temperature profile, whilst variations over the last 200-300 years will affect the upper 200 m, and post-glacial
285 warming can be observed down to 2500 m. These effects are dampened by an overlying water column or ice sheet,
286 but temperature variation over 10 kyr can still affect basal ice sheet temperatures (Engelhardt, 2004). Whilst large
287 ($> 10^\circ\text{C}$) seasonal temperature variations are dampened by $\sim 90\%$ at water depths of 3-5 m (Müller et al., 2016),
288 long-term variations (e.g. climate-controlled variations in Circumpolar Deep Water over the last ~ 12 kyr;
289 Hillenbrand et al., 2017) are likely recorded in the upper 3 m at 400 m water depth, 2 m at 700 m depth, and even
290 the upper ~ 1 m at 1000 m depth (Dziadek et al., 2019).

291 Similarly to borehole temperature measurements, a time delay must be considered between penetration of the
292 sediments and temperature measurement. A ten minute delay between sediment penetration and measurement is
293 sufficient to allow decay of frictional heating, as the temperature decay takes $\sim 100 \text{ s}$ (Dziadek et al., 2019; Pfender
294 and Villinger, 2002).

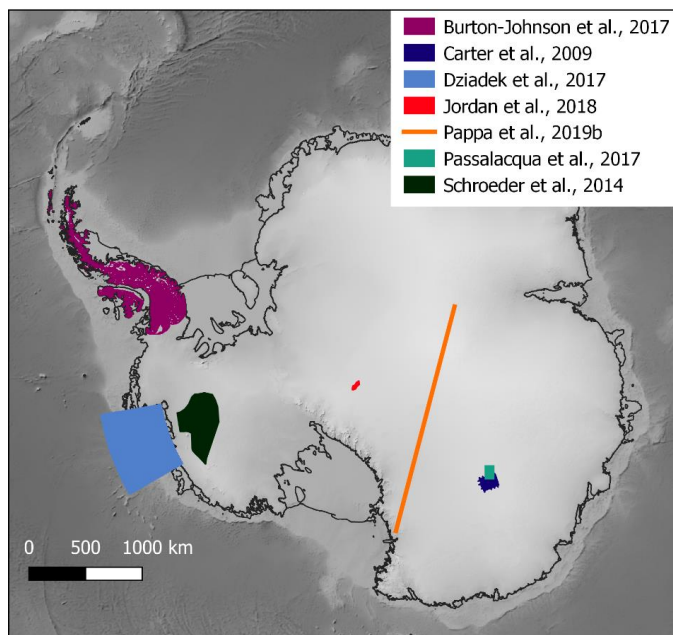


295 **4. Geophysical and geological methods to estimate GHF**

296 In addition to the few and sparse penetrative GHF estimates in Antarctica, continental (Fig. 5) and regional (Fig.
297 6) estimates have been derived from both solid Earth (geophysical/geological), and glaciological data and models.



298 c, Shapiro & Ritzwoller 2004
299 **Fig. 5. Continent-scale geophysical estimates of GHF derived from magnetic Curie depth estimates (a and b; Fox Maule**
300 **et al., 2005; Martos et al., 2017a) and seismic models (c and d; An et al., 2015a; Shapiro and Ritzwoller, 2004).**



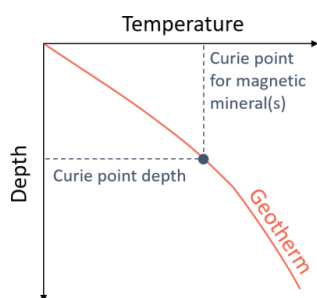
301

302 **Fig. 6. Coverage of sub-continental scale regional estimates of GHF.**

303 4.1. Magnetic methods deriving GHF from Curie depth

304 As for the penetrative methods of GHF estimation described above (Section 3), geophysical methods also derive
305 GHF from a temperature gradient. In this case, magnetic survey data is used to determine the depth at which the
306 maximum temperature of ferromagnetic magnetisation is exceeded (the Curie temperature; Haggerty, 1978). This
307 Curie temperature is different for different minerals, but is assumed in these studies to the Curie temperature of
308 magnetite (580 °C) as this mineral is most commonly the dominant contributor to crustal magnetisation (Bansal
309 et al., 2011; Fox Maule et al., 2005; Langel and Hinze, 1998).

310 Above the Curie temperature, rocks lose their ability to maintain ferromagnetic magnetisation (e.g. Haggerty,
311 1978). The depth of this isotherm in the crust (the Curie Point Depth, CPD; Fig. 7 and Fig. 2) is thus assumed to
312 be the depth to the bottom of the magnetic source (DBMS) determined from magnetic survey data. The DBMS
313 maps a transition zone, rather than an exact depth (Haggerty, 1978), and can provide information on crustal
314 temperatures at depths not accessible by other means (Andrés et al., 2018; Okubo et al., 1985). Regions found to
315 have a shallower DBMS (and thus an assumed shallower CPD) are expected to have higher average temperature
316 gradients, and, therefore, higher GHF (e.g. Aboud et al., 2011; Andrés et al., 2018; Arnaiz-Rodríguez and
317 Orihuela, 2013; Bansal et al., 2013, 2011; Bhattacharyya and Leu, 1975; Guimarães et al., 2013; Li et al., 2017;
318 Obande et al., 2014; Okubo et al., 1985; Ross et al., 2006; Salem et al., 2014; Tanaka et al., 1999; Trifonova et
319 al., 2009).



320

321 **Fig. 7. Approximation of the geothermal gradient from the Curie point depth (CPD). The Curie point depth is assumed**
322 **to mark the base of the magnetic crust (DBMS).**

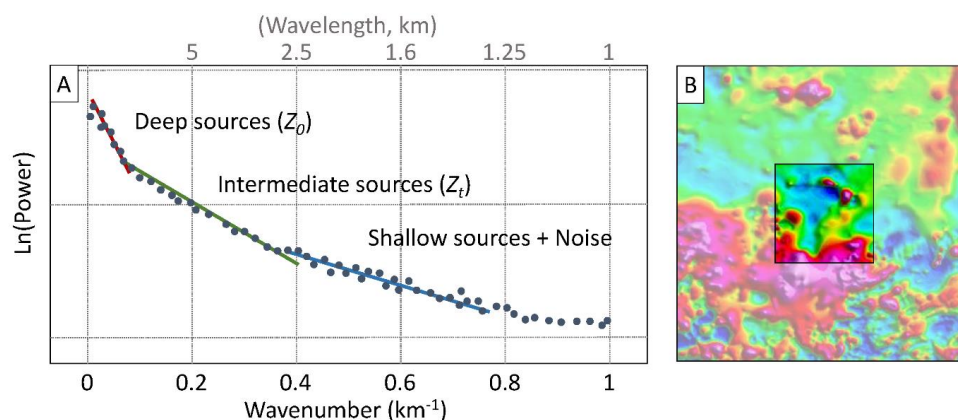
323 The first Antarctic-wide magnetically-derived GHF map (Fox Maule et al., 2005; Fig. 5a) used the “equivalent
324 source magnetic dipole method” (Mayhew, 1979) to map magnetic anomalies from multiple satellites at different
325 altitudes as evenly distributed magnetic dipoles on the Earth’s surface (Dyment and Arkani-Hamed, 1998). Due
326 to filtering of the data during processing, this magnetic anomaly distribution is only susceptible to shallow, short-
327 wavelength magnetic variation. To calculate the CPD, a long-wavelength CPD model was modified until it
328 reproduced the determined short-wavelength anomalies. The temperature gradient represented by this CPD was
329 combined with assumed homogenous crustal properties (heat production and conductivity) to model the surface
330 heat flow. Due to the high altitude of the satellite data, the horizontal resolution of this approach was limited to at
331 least a few hundred kilometres.

332 Spectral methods are the alternative and more commonly applied approach to estimating the DBMS, analysing
333 the spectrum of wavelengths in magnetic profiles or gridded data (e.g. Blakely, 1996; Okubo et al., 1985; Spector
334 and Grant, 1970). These methods depend on the implicit assumption that long wavelength features result from
335 deep sources. The depth of this source is calculated from a “power spectrum” (Fig. 8) of wavenumber (the inverse
336 of the wavelength) against the logarithm of each wavenumber’s “power” (the square of each wavelength’s
337 magnitude after conversion by a Fast Fourier Transformation to describe the spectrum of wavelengths in the
338 signal). From this power spectrum (Fig. 8) the top (Z_t) and centre (Z_0) of the deepest magnetic layer are inferred
339 from the slope of the intermediate and long wavelength zone of the spectra derived from magnetic anomaly data.
340 The DBMS (Z_{DBMS}) stems from the simple geometric relationship between these depths:

341

$$Z_{DBMS} = 2Z_0 - Z_t$$

342 (6)



343

344 **Fig. 8. A) Identification of the slopes of the intermediate and long wavelength magnetic anomalies from the power**
345 **spectrum of magnetic anomalies within a single magnetic window (B). For illustration, small circular anomalies in the**
346 **magnetic window (B) would correspond to shallow sources in the power spectrum, whilst larger anomalies would**
347 **correspond to intermediate and deep sources.**

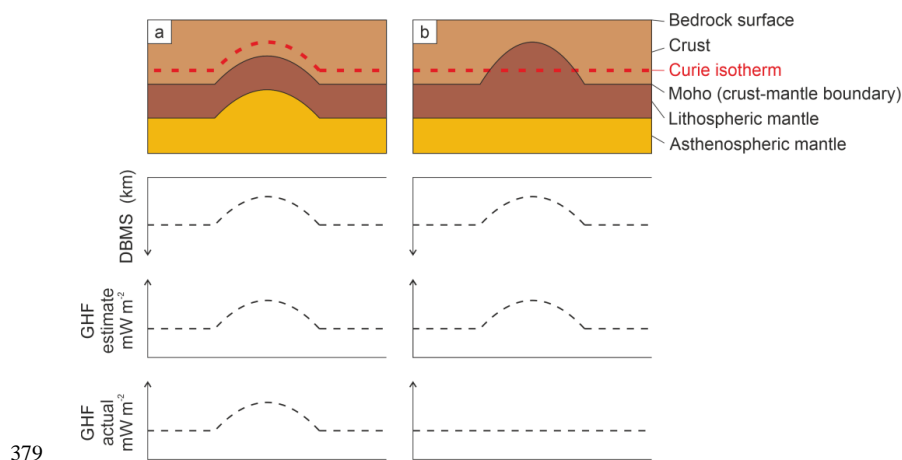
348 To map the DBMS across a study area, the spectra of magnetic anomalies are computed within overlapping
349 rectangular windows regularly spaced over the aeromagnetic map. Particularly for gridded data, the dimensions
350 of the region chosen to analyse the long wavelength frequencies must be sufficiently large to capture the DBMS.
351 Ravat et al. (2007) elaborate that the dimension of the region analysed may need to be (in some cases) up to 10
352 times the DBMS, but that dimensions exceeding 200 to 300 km may average different large-scale crustal
353 structures. This suggests that satellite data, which typically detects magnetic anomalies in that wavelength, may
354 not be suitable for this spectral method of CPD estimation. Choosing the window size therefore forces a trade-off
355 between accurately determining the DBMS within each sub-region and resolving small changes in DBMS between
356 sub-regions (Ross et al., 2006).

357 Spectral methods have been applied in Antarctica (Dziadek et al., 2017; Martos et al., 2017a; Purucker and
358 Whaler, 2007; Fig. 5b and Fig. 6) to combined satellite and airborne magnetic anomaly data (e.g. ADMAP;
359 Golynsky et al., 2006; Maus, 2010). The results show a general agreement at a continental scale, but vary
360 significantly on a regional scale (Fig. 5). This is related to the resolution of the magnetic anomaly data, particularly
361 in regions where only satellite magnetic data are available. Furthermore, regional-scale magnetic anomaly
362 databases are usually a mosaic of individual aeromagnetic surveys. Ross et al. (2006) emphasise that subtle
363 discontinuities along survey boundaries are caused by differences in survey specifications, such as flight line
364 spacing, flight altitude, regional field removal, or the quality of data acquisition. These, for instance, may
365 contaminate the long-wavelength signal caused by deep magnetic sources (Grauch, 1993). Long wavelength
366 features can also result from shallow but spatially extensive sources, such as volcanic provinces, and can lead to
367 an underestimation of the DBMS.

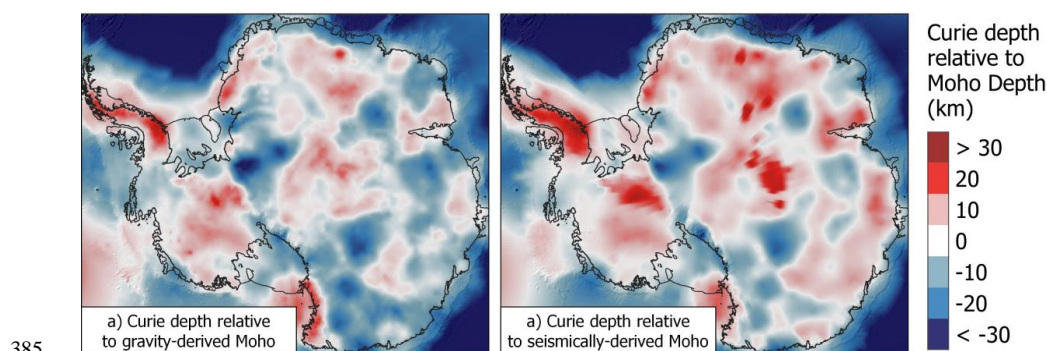
368 CPD estimates assume a homogenous magnetic mineralogy of magnetite, and thus a Curie temperature of 580 °C
369 (Bansal et al., 2011; Fox Maule et al., 2005; Langel and Hinze, 1998). This assumption neglects the compositional
370 variability in plutonic rocks that lead to Curie temperature ranges between 300 °C and 680 °C, and in cases of



371 magnetic assemblages of Fe-Ni-Co-Cu metal alloys up to 620 °C to 1084 °C (Haggerty, 1978). Without further
 372 constraints and validations, these assumptions remain the best approach, especially in sparsely sampled regions
 373 like Antarctica, but introduce uncertainties of several kilometres in Curie depths and consequent uncertainties in
 374 GHF estimates (Bansal et al., 2011; Ravat et al., 2007). Similarly, in areas of thin crust, non-magnetic mantle
 375 rocks can be shallower than the Curie depth. In these regions, the calculated Curie isotherm will appear shallower
 376 due to a lack of magnetic minerals in the mantle rocks (Fig. 9.; Frost and Shive, 1986; Wasilewski and Mayhew,
 377 1992). This can be investigated through comparison of the Antarctic Curie depth estimates with the seismically-
 378 or gravitationally-derived depth of the crust-mantle boundary (the Moho depth; Fig. 10 and Fig. 2).



379
 380 **Fig. 9.** Two scenarios illustrating the ambiguity in estimating Curie isotherm depth and GHF. a) Estimates from a
 381 region with a shallow Curie isotherm over an area of thin crust. b) Similar but incorrectly interpreted estimates from
 382 a region of shallow non-magnetic mantle rocks. In scenario (b), the DBMS is shallower despite there being no deviation
 383 in the Curie isotherm depth. DBMS – Depth to the Bottom of the Magnetic Source (assumed to represent the Curie
 384 depth in the GHF estimates discussed).



385
 386 **Fig. 10.** Comparison of Curie depth (Martos et al., 2017) and depth of the crust-mantle boundary (the Moho depth)
 387 derived from a) gravity modelling (Pappa et al., 2019b), and b) seismic modelling (An et al., 2015a). Negative values
 388 show areas where the estimated Curie depth is deeper than the estimated Moho depth, and positive values are where
 389 the Curie depth is shallower than the Moho depth.



390 However, whilst in general the Earth's mantle does not contribute to the magnetic signal (due to its weak
391 magnetisation and high temperature conditions), in some cases the Curie depth may indeed lie within the mantle.
392 This occurs where metallic magnetic phases in the mantle beneath old, tectonically stable crust ("cratons"; Ferré
393 et al., 2013) or subduction regions (e.g. Blakely et al., 2005) contribute to mantle magnetisation. In these settings
394 the crust-mantle boundary should not be considered an absolute magnetic boundary (Ferré et al., 2013). This
395 implies that if in a given region the Moho depths are shallower than the deepest magnetic layer, a magnetic mantle
396 at temperatures below the Curie temperature may be considered. However, even in these cases the upper mantle
397 susceptibility will be more than 1-2 magnitudes smaller than the overlying crust. This is not considered in current
398 spectral methods assuming constant susceptibility. Consequently, Curie depth methods yield non-unique
399 solutions, and further available constraints and observations need to be considered, when interpreting the Curie
400 temperature distribution (e.g. geological evidence, borehole measurements, and Moho depth estimates).

401 4.2. Seismic estimates

402 Temperature is the dominant control on seismic velocity in the mantle (e.g. Carlson et al., 2005), and hence the
403 mantle heat flow at the base of the Antarctic crust can be determined from seismic data. By determining the change
404 in seismic velocities marking the density discontinuity at the lithosphere-asthenosphere boundary (Fig. 2) the
405 depth of the 1330°C isotherm can be estimated. This is the "mantle adiabat" marking the top of the seismic low-
406 velocity zone, and the change from a solid to ductile mantle (Fig. 2). The continental-scale GHF can then be
407 estimated by assuming the heat production and conductivity of the lithosphere above this boundary, and
408 integrating this with the seismically-derived mantle heat flow (An et al., 2015b; Fig. 5d). However, the
409 seismically-derived, continent-scale Antarctic GHF model of An et al. (2015a) (Fig. 5d) is limited to a lateral
410 spatial resolution of >120 km, assumes a laterally uniform crustal structure, and is insensitive to the lithospheric
411 geotherm (instead it inversely correlates with crustal thickness).

412 Composition also affects seismic velocities. For example, a 2% increase in velocity can be explained either by a
413 120°C decrease in temperature, a 7.5% depletion in iron, or a 15% depletion in aluminium (Godey et al., 2004).
414 Slow mantle velocities at subduction zones can also be caused by water or hydrous fluids serpentinising the mantle
415 wedge (Fig. 2; Kawakatsu and Watada, 2007). However, velocity in the Antarctic seismic model (An et al., 2015b)
416 does not account for variability of mantle compositions, mineralogy, grain size, or water content of the mantle or
417 crust. An uncertainty in the lithospheric thickness of 15-30 km was assumed by (An et al., 2015b) based on the
418 150°C temperature uncertainty, but ~50 km uncertainty for ~200 km thick lithosphere may be more accurate
419 (Artemieva, 2011; Godey et al., 2004). In addition, seismological models suffer from limited and inconsistent
420 spatial coverage, which can lead to discrepancies in upper mantle velocities and differences in Moho depths (Fig.
421 2) up to 10 km, even for the same receiving station (An et al., 2015b supporting information; Pappa et al., 2019).

422 Some constraints on the mantle and lithosphere composition can be determined from xenoliths (rock fragments
423 of the deep crust or mantle entrained in magma rising from depth) or exposed deep crustal sections, where
424 variation in temperature and composition with depth can be determined from the metamorphic minerals present.
425 Constraints can also be derived empirically by comparing the seismic velocity with similar regions. Shapiro and
426 Ritzwoller (2004) (Fig. 5c) extrapolated global heat flow measurements to Antarctica based on the assumption
427 that structurally similar regions have similar magnitudes of GHF. This was achieved by calculating a spatially



428 variable “similarity functional” determined from the differences between the seismic velocity and seismic Moho
429 depth between a location of interest and a comparable location elsewhere. A histogram of heat flow measurements
430 could then be assigned to the location of interest in Antarctica based on the similarity-weighted sum of
431 measurements from structurally similar regions, and the mean values of these distributions mapped as continental
432 heat flow. Spatial resolution was limited to the lateral resolution of the global shear velocity model across
433 Antarctica (600-1000 km; Shapiro and Ritzwoller, 2002). Although the studies of Shapiro and Ritzwoller (2004)
434 and An et al. (2015a) both used seismic data and are thus frequently compared, it is important to highlight that
435 they use very different approaches in deriving heat flow (the former employing a probabilistic approach and the
436 latter using forward modelling).

437 4.3. Gravity modelling

438 Satellite gravity data has been used as an alternative to seismic modelling to determine crustal thickness. Pappa
439 et al. (2019b) used satellite gravity data, a model of global gravity variation (the “geoid”), surface and bedrock
440 topography, and assumed rock and ice densities to calculate the topographically-corrected variation of gravity in
441 Antarctica (the “Bouguer anomaly”), from which the depth of the crust-mantle boundary could be calculated. This
442 approach to calculate crustal thickness is sensitive to long-wavelength (>150 km) features representing deep
443 structures, rather than short-wavelength, near surface density changes. However, gravity-modelling solutions are
444 non-unique, and require additional constraints on the density contrast between the crust and mantle at a reference
445 depth, and/or seismic depth constraints on crustal thickness.

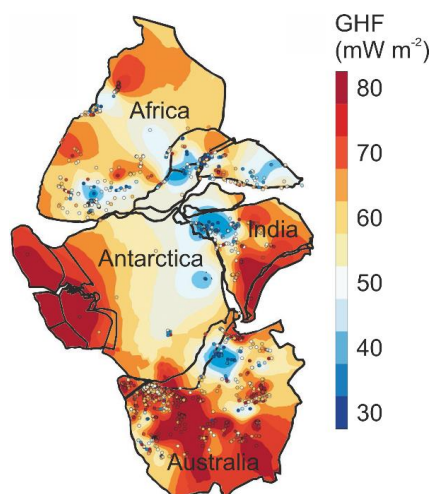
446 Using the gravity-derived crustal thickness estimates, cross-sectional models of the mantle and lithospheric
447 structure were calculated, with adjustments made to crustal density and crustal thickness until the models reflected
448 the observed variation in gravity and elevation (Pappa et al., 2019b). By assigning assumed values of heat
449 productivity and thermal conductivity values to the modelled cross-sections, surface heat flow was calculated
450 along the line of the modelled cross-section (Fig. 6). A 3D lithospheric model has since been published (Pappa et
451 al., 2019a), and a map of Antarctica’s resultant estimated GHF is in preparation for publication (pers. comms.).

452 4.4. Conjugate margins

453 An alternative approach to constrain the probable GHF of East Antarctica is to compare it with its Gondwanan
454 conjugate margins, reconstructed prior to the breakup of the supercontinent (Fig. 11). Plate tectonic
455 reconstructions indicate that the subglacial geology of East Antarctica is comparable to the margins of Australia,
456 Africa, and India (Aitken et al., 2016; Daczko et al., 2018; Ferraccioli et al., 2011; Flowerdew et al., 2013; Mulder
457 et al., 2019). By kriging the heat flow measurements of the continents in their pre-Gondwana breakup
458 arrangement, Pollett et al. (2019) interpolated a heat flow surface through Antarctica and its conjugate margins
459 (Fig. 11). This method highlighted similarities and differences between the most recent seismic and magnetically
460 derived geophysical models of Antarctic heat flow (An et al., 2015b; Martos et al., 2017) with the better
461 constrained heat flow of the conjugate margins. In particular, this approach showed reasonable agreement along
462 the margin with Africa, but an absence in either the magnetic or seismic models of high heat flow provinces in
463 East Antarctica comparable with south Australia; an absence of the low heat flow of SW Australia in the
464 magnetically derived model of East Antarctica (Martos et al., 2017); and an absence of the high heat flow of



465 northern India in the seismically derived model of East Antarctica (An et al., 2015b). However, when extrapolating
 466 heat flow away from the conjugate margins into the interior of Antarctica, this approach is susceptible to the
 467 method of interpolation used and the quality and scarcity of the borehole-derived GHF estimates in the interior of
 468 Antarctica (Section 3).

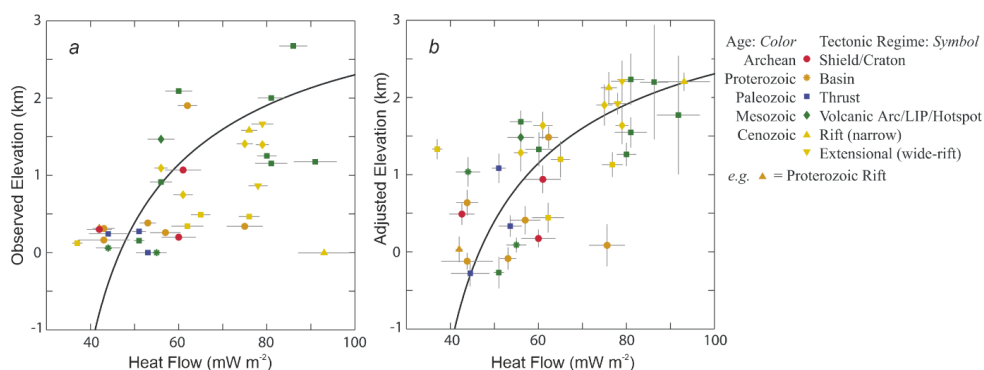


469

470 **Fig. 11.** Interpolated heat flow map of Gondwana, showing the derivation of Antarctic GHF from the reconstructed
 471 conjugate margins of the supercontinent. Terrestrial heat flow data shown by points. Adapted from Pollett et al. (2019).

472 4.5. Isostatic elevation

473 In addition to crustal thickness and density, the thermal state of the lithosphere also contributes to its isostasy and
 474 observed surface elevation. The effect of thermal isostasy on the bathymetry of oceanic crust is well recognised:
 475 as oceanic crust migrates from the spreading ridge it cools, thickens, contracts, and subsides (Stein and Stein,
 476 1992). However, the effect of thermal isostasy on continents is masked by compositional contributions to isostatic
 477 elevation (i.e. lateral variations in crustal thickness and density, Fig. 12a; Hasterok and Chapman, 2007b, 2007a).



478

479 **Fig. 12.** Relationship of the median observed (a) and adjusted (b) elevation and median compiled heat flow values of 36
 480 geological provinces on the land and continental shelves of North America, ranging from 30 - 2082 x 10³ km². Compiled



481 heat flow data excluded values outside of the range 20 - 120 mW m⁻² as these values were most likely affected by near
482 surface processes (e.g. hydrothermal circulation) or shallow magmatism, and do not reflect the lithosphere's thermal
483 state. Observed elevations are converted to adjusted elevation by normalising according to their seismically-derived
484 crustal thickness and crustal density and an equation for thickness and density-based isostasy. The black curve shows
485 the best-fitting thermal-isostatic model for North American adjusted elevation and heat flow. Adapted from Hasterok
486 and Chapman (2007a).

487 Hasterok and Chapman (2007b, 2007a) developed a methodology for investigating thermal isostasy in the
488 continental lithosphere by normalising the observed elevation using an isostatic correction. The normalised
489 elevation (ε') is calculated from Equation 7 (Han and Chapman, 1995):

$$490 \quad \varepsilon' = \varepsilon + h'_c \left(1 - \frac{\rho'_c}{\rho_m}\right) - h_c \left(1 - \frac{\rho_c}{\rho_m}\right)$$

491 (7)

492 Where ε is the observed elevation; h_c and ρ_c are respectively the seismically-derived crustal thickness and density
493 of the study area; h'_c and ρ'_c are the thickness and density respectively of a standard crustal column; and ρ_m is
494 the mantle density. When the crust is below sea level, an additional term including bathymetric water depth (ε_{obs})
495 and seawater density (ρ_w) are included (Equation 8; Han and Chapman, 1995):

$$496 \quad \varepsilon' = \varepsilon + h'_c \left(1 - \frac{\rho'_c}{\rho_m}\right) - h_c \left(1 - \frac{\rho_c}{\rho_m}\right) - \left(\frac{\varepsilon_{obs}\rho_w}{\rho_m}\right)$$

497 (8)

498 Compositionally corrected elevation generally increases with increasing surface heat flow (Fig. 12b). By
499 differentiating the different contributions to isostatic elevation, it was shown that crustal thickness and density
500 contribute ~3 km of the observed elevation range of North America, and thermal isostasy contributes a further ~3
501 km; similar in magnitude to the effect of thermal isostasy on oceanic lithosphere (Hasterok and Chapman, 2007a,
502 2007b). However, there are uncertainties in the thermal isostasy model associated with the assumed properties,
503 including thermal conductivity, thermal expansion, and heat production in the upper and lower crust, of which
504 uncertainty in upper crustal heat production has the largest effect (Hasterok and Chapman, 2007b). Uncertainties
505 in the seismic data used for calculating crustal thickness and density affect the uncertainty of the compositional
506 isostatic correction (Equations 7 and 8; Hasterok and Chapman, 2007b).

507 This approach was used to derive the thermal contribution to isostatic elevation of Australia and North America,
508 and estimate the continental sub-lithospheric and radiogenic heat flow (Hasterok and Chapman, 2007b; Hasterok
509 and Gard, 2016). Whilst in general, the compositionally corrected elevation and surface heat flow values followed
510 the modelled curve for thermal isostatic equilibrium (Fig. 12b), anomalous regions lie away from this curve. These
511 anomalies result from: 1) additional sources of buoyancy and/or dynamic support (e.g. anomalously buoyant
512 mantle lithosphere); 2) anomalous surface heat flow, not representative of the deeper thermal regime (e.g. high
513 concentration of heat producing elements in the shallow crust); 3) deviations from the thermal properties of the
514 reference crustal model (e.g. heat production); or 4) combinations of these properties (Hasterok and Gard, 2016).



515 Although developed for regions of known heat flow, application of this approach to Antarctica (Hasterok et al.,
516 2019) may provide an alternative estimate of heat flow based largely on two well-constrained variables: surface
517 and bedrock topography. However, it is dependent on the quality of seismic constraints on crustal thickness and
518 density as well as constraints on the heat production and thermophysical properties of the upper crust. For
519 example, regions where high surface heat flow is dominantly from anomalously high upper crustal heat production
520 will have lower elevations than regions of similar surface heat flow but with lower upper crustal heat production.
521 Crust that has experienced tectonic and magmatic activity in the Cenozoic (i.e. <66 Ma) may be in a transient
522 rather steady-state thermal regime, so this approach may have challenges in West Antarctica. Steady-state thermal
523 modelling is thus more applicable to the old, stable crust of East Antarctica; particularly if the heat flow and
524 isostasy of the conjugate margins are considered (Hasterok and Gard, 2016; Pollett et al., 2019). However,
525 differences between the crustal thickness based on gravity modelling and isostatic elevation modelling may
526 indicate variable densities and/or compositions of the underlying mantle (Pappa et al., 2019b, 2019a).

527 4.6. Enhancement of GHF estimates by incorporation of heterogeneous crustal compositions

528 The geophysical approaches described above assume laterally homogenous heat production in the crust. However,
529 given the geologically heterogeneous composition of the crust, it is important to consider the effects of variable
530 lithospheric heat production and incorporate this into forward models of GHF.

531 Radiogenic heat production in the upper crust contributes an estimated 26-40 % of the total continental GHF
532 (Artemieva and Mooney, 2001; Hasterok and Chapman, 2007b, 2011; Pollack and Chapman, 1977; Vitorello and
533 Pollack, 1980). Radioactive isotopes of the heat producing elements (HPEs) uranium, thorium, and potassium (U,
534 Th, and K) are responsible for ~98% of lithospheric heat production (Beardsmore and Cull, 2001). These elements
535 are incompatible with mineral structures in the mantle and lower crust, so concentrate in the upper crust and
536 decrease in abundance with depth during planetary differentiation (the chemical and physical separation of an
537 initially homogenous planetary body into one with an iron-rich core, magnesium-silicate-rich mantle, and a thin
538 silicate-rich crust; Roy et al., 1968; Rudnick and Fountain, 1995).

539 The upper crust itself is highly heterogeneous in composition. HPE distribution is determined by their
540 compatibility in different minerals, concentrating them in Si-rich silicic rocks (e.g. granite or rhyolite) relative to
541 Fe-rich mafic rocks (e.g. gabbro or basalt). Immature sediments inherit the HPE abundance of their eroded source
542 rocks, but decrease in HPE abundance with increasing maturity and the consequent decrease in their lithic contents
543 (Burton-Johnson et al., 2017; Rybach, 1986). Crustal heat production is thus heterogeneous, and the most
544 significant control of HPE abundance and resultant heat production in the lithosphere is the distribution of the
545 composite lithologies of the upper crust (Lachenbruch, 1968; Sandiford and McLaren, 2002; Taylor and
546 McLennan, 1985).

547 4.6.1. Whole rock geochemical analysis of heat production

548 Heat production of exposed lithologies can be determined from their concentrations of HPE (U, Th, and K)
549 determined by geochemical analysis, or by airborne or ground-based gamma ray surveys. Radiogenic heat
550 production for each sample (H , μWm^{-3}) for the present day ($t=0$) can be determined from Equation 9 (Turcotte
551 and Schubert, 2014):



552
$$H = (0.9928C_0^U H^{U238} + 0.0071C_0^Th H^{U235} + C_0^{Th} H^{Th232} + 0.000119C_0^K H^{K40})D$$

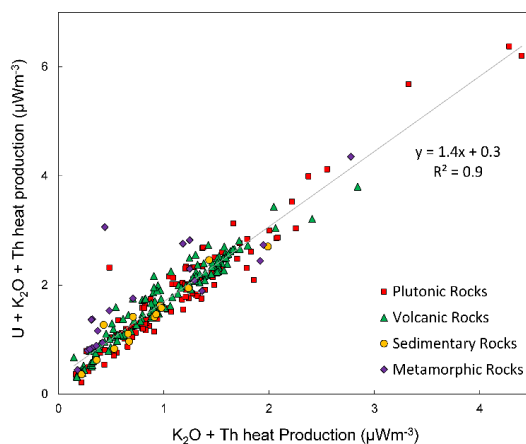
553 (9)

554 Where C_0^U , C_0^{Th} and C_0^K are the measured concentrations (ppm) of U, Th and K respectively; H^{U238} , H^{U235} , H^{Th232}
 555 and H^{K40} are the heat productivities of the respective isotopes ^{238}U ($9.37 \times 10^{-5} \text{ Wkg}^{-1}$), ^{235}U ($5.69 \times 10^{-4} \text{ Wkg}^{-1}$),
 556 ^{232}Th ($2.69 \times 10^{-5} \text{ Wkg}^{-1}$) and ^{40}K ($2.79 \times 10^{-5} \text{ Wkg}^{-1}$); and D is the assumed density of the rock (e.g. 2800, 2850,
 557 and 3000 kg m^{-3} for felsic, intermediate, and mafic granulites, respectively; Hasterok and Chapman, 2011). When
 558 using geochemical data to calculate heat production, this allows new and archive data to be used to calculate the
 559 heat production of the sampled outcrop. However, many archive analyses occurred prior to the development of
 560 accurately U quantification (e.g. by high resolution XRF or ICP-MS). An empirical relationship (Equation 10;
 561 Burton-Johnson et al., 2017) allows calculation of total U, Th, and K heat production (H) from samples possessing
 562 only Th and K data ($H_{K,Th}$; correlation coefficient, $R^2 = 0.9$; Fig. 13).

563
$$H = 1.4H_{K,Th} + 0.3$$

564 (10)

565 Heat production values can be assigned to bedrock geology either by interpolation of the point values or by
 566 assigning the point values to the mapped geology and assigning their average value to the geological unit; the
 567 average being either the mean (Veikkolainen and Kukkonen, 2019), area weighted mean (Slagstad, 2008), or
 568 median value (Burton-Johnson et al., 2017). Interpolation shows spatial variability within a unit, but is affected
 569 by the interpolation method used, requires sufficient and evenly distributed data coverage, and is affected by
 570 anomalous values. For these reasons, the median values were used for the unevenly distributed archive data of the
 571 Antarctic Peninsula (Burton-Johnson et al., 2017). In Antarctica, this approach has been applied to the Antarctic
 572 Peninsula (Burton-Johnson et al., 2017; Fig. 6) and along coastal outcrops in East Antarctica (Carson et al., 2014;
 573 Carson and Pittard, 2012). These studies integrated their maps of variable lithospheric heat production with
 574 geophysical models of the deeper heat flow to estimate the total GHF at the bedrock surface.



575



576 **Fig. 13. The relationship between total calculated heat production from U, K₂O and Th decay and the heat production**
577 **values from K₂O and Th only for different broad lithologies, enabling total heat production calculation from incomplete**
578 **archive data (n = 319; Burton-Johnson et al., 2017).**

579 **4.6.2. Gamma ray spectrometry**

580 Rather than whole rock geochemical analysis, the gamma ray spectrum can be used to determine the
581 concentrations of radioactive isotopes, including those of K, Th, and U, and was first used for U exploration.
582 Gamma ray spectrometry can be surveyed in the field, on samples, or from the air. Airborne surveys can cover
583 large areas, and have been used to survey Western Australia, SW England, and all of Finland (Beamish and Busby,
584 2016; Bodorkos et al., 2004; Hyvönen et al., 1972). However, the data requires multiple corrections, and the
585 recorded data integrates the radiation from the bedrock, surface cover (including soil and vegetation), the
586 atmosphere, cosmic radiation, and the aircraft, making the data less accurate than ground measurements or sample
587 analysis (Veikkolainen and Kukkonen, 2019). The technique is only sensitive to the upper 25cm of the land
588 surface, with overlying sediments and water bodies masking the radiation and leading to underestimates of heat
589 production (Phaneuf and Mareschal, 2014). However, if the signal could be linked to mapped geological units and
590 other evidence for subglacial geology (e.g. aeromagnetic and gravity anomalies) it may be feasible to extrapolate
591 the calculated heat production beneath the ice sheet. Hand-held gamma ray spectrometry studies, where heat
592 production can be correlated with lithology along exhumed crustal profiles, show promise in this regard elsewhere
593 (Alessio et al., 2018).

594 **4.6.3. Crustal structure**

595 Whilst surface HPE distribution can be constrained by measurements, the vertical distribution is more ambiguous.
596 In heat flow models, heat production is often assumed to decrease exponentially with depth (e.g. Fox Maule et al.,
597 2005; Martos et al., 2017). This exponential model was developed to explain observations from exposures of
598 large, thick composite granite bodies (batholiths) where magma was initially emplaced at different depths in the
599 crust (Lachenbruch, 1968, 1970; Swanberg, 1972) and reflects a proposed decrease in HPE abundance with
600 increasing metamorphic grade (Lachenbruch, 1968; Sandiford and McLaren, 2002). However, this relationship
601 has been challenged by other studies comparing HPE abundance and metamorphic grade (Alessio et al., 2018;
602 Veikkolainen and Kukkonen, 2019), showing that the lithological change from the largely silicic upper crust to
603 the mafic lower crust has a larger influence on HPE abundance than metamorphic grade (Bea, 2012; Bea and
604 Montero, 1999). Deep (9-12 km) boreholes also show a correlation of heat production with lithology, but not with
605 depth (Clauser et al., 1997; Popov et al., 1999). In fact, heat production *increased* for the first 2 km of the 12 km
606 superdeep well of the Kola Peninsula, Russia, then remained variable but high with increasing depth (Popov et
607 al., 1999). Similarly, heat production increases below 3 km in the recent 5 km UD-1 well of the Cornubian
608 Batholith, UK (Dalby et al., 2020). As such, the available evidence indicates that the first-order HPE distribution
609 is controlled by the HPE abundance of the crust prior to metamorphism and the vertical distribution of the crust's
610 composite rock types. Inversely, it indicates that HPE distribution is not controlled by depth in the crust or the
611 degree of metamorphism resulting from the increase in pressure and temperature.

612 Without evidence for the deeper structure of the crustal column, the lithological and HPE distribution of the
613 lithosphere can instead be modelled as layers of variable thickness and heat production: the upper crust, middle



614 crust, lower crust, and mantle lithosphere. Surface heat flow is largely insensitive to variations in the heat
615 production or thickness of the mafic lower crust and mantle lithosphere due to their heat production being ~1-2
616 orders of magnitude lower than that of the upper crust (Hasterok and Chapman, 2011; Rudnick and Fountain,
617 1995; Rudnick et al., 1998). The middle crustal layer can either be excluded (Hasterok and Chapman, 2011) or
618 treated as a layer of invariable heat production (e.g. An et al., 2015, for Antarctica) due to its low heat production
619 compared with the range of the upper crust. Lithospheric heat production can thus be defined by the heat
620 production and relative thickness of the upper crust, or upper crustal heat producing layer (Hasterok and Chapman,
621 2011). This can be defined by:

$$Q_s = Q_b + H_{UC}D = FQ_s + H_{UC}D = H_{UC}D/(1 - F)$$

622
623 (11)

624 Where Q_s is the surface heat flow, Q_b is the basal heat flow of the upper crust, H_{UC} is upper crustal heat production,
625 D is the thickness of the upper crustal heat producing layer, and F is the proportion of the surface heat flow
626 contributed by the basal heat flow (Q_b) (adapted from Hasterok and Chapman, 2011).

627 Rather than a simple layered model, more complex 2D or 3D models of upper crustal structure can be developed
628 using geophysical data, and the 2D or 3D crustal units assigned heat production and conductivity values based on
629 analyses of representative exposures. A 3D crustal model derived from gravity and aeromagnetic data was
630 developed to map heat flow in Norway (Ebbing et al., 2006; Olesen et al., 2007). In Antarctica, this has been
631 applied in 2D to the high heat production granites of the Ellsworth-Whitmore Mountains using airborne magnetic
632 and gravity data and bedrock topography (Leat et al., 2018), and the Transantarctic Mountains using topography
633 and satellite gravity data (Pappa et al., 2019b).

634 Whilst variability in deep lithospheric heat production has a smaller effect on surface heat flow than variability in
635 upper crustal heat production (Hasterok and Chapman, 2011), it is not homogenous. These thermophysical
636 properties can be constrained from deep xenoliths (fragments of rock entrained in magma rising from depth)
637 (Hasterok and Chapman, 2011; Martin et al., 2014) and crustal sections (Berg et al., 1989), which can also inform
638 on the local geothermal gradient at the time of their crystallisation.

639 To help constrain the properties of the Antarctic mantle, including its influence on Antarctic heat flow, a
640 Geological Society of London Memoir is currently being compiled summarising the data gained from mantle
641 xenoliths (Martin and van der Wal, in prep.). This includes a sample database, and a compilation of their grain
642 size and water content. These xenoliths are from shallow sources, as their occurrence is biased towards areas of
643 crustal rifting where the lithosphere is thinner, although some xenoliths are from deeper sources (e.g. from the
644 Amery Rift and Ferrar Dolerite).

645 4.6.4. Detrital material

646 Whilst heat production can be determined for exposed bedrock, the likely heat production of the rocks beneath
647 the Antarctic ice sheet is harder to constrain. To investigate East Antarctica, glacial clasts were sampled from
648 moraines adjacent to the Transantarctic Mountains (Goode, 2018). Granitic samples older than 500 Ma (Ross
649 Orogen) were selected as likely lithologies of the interior of East Antarctica, as these are the dominant lithologies



650 of other Precambrian cratons (>542 Ma regions of tectonically-stable continental crust; e.g. central Canada). These
651 clasts were analysed for their HPE abundance and attributed to their likely source area (the drainage basin of their
652 associated glaciers). A probable range of subglacial heat flow values was estimated by assuming mantle and lower
653 crustal GHF values and a thickness for the upper crust based on other Precambrian shields. This indicates that
654 East Antarctic heat flow is comparable to other Precambrian cratons, and comparable to geophysical models of
655 East Antarctic heat flow (Liefvering and Pattyn, 2013). However, broader application of this approach is biased
656 towards more erosion resistant rock types, whilst less competent lithologies will not be preserved after glacial
657 transport and deposition.

658 **5. Glaciological inverse estimation of GHF**

659 Although geothermal heat flow has a geological derivation, it can also be constrained by multiple approaches
660 through its observable effects on the overlying ice sheet. Rather than using a forward modelling approach (i.e.
661 determining the geological contributions and estimating their resultant heat flow), an inverse modelling approach
662 can be applied by modelling observed glaciological properties (e.g. glacial flow and melt rates) and calculating
663 the required heat flow. We will describe in this section different methods used in glaciology to derive GHF.

664 **5.1. Subglacial water**

665 The presence of subglacial water can be detected with a ground penetrating radar. The reflective properties of the
666 ice-bedrock interface depend on the presence of water and, with certain caveats, radar surveys can be used to map
667 subglacial water. In general terms, a glaciological model can then be used to estimate the values of GHF that
668 better predict where basal temperatures reach the pressure melting point and melting occurs. We will describe in
669 this Section examples of this approach.

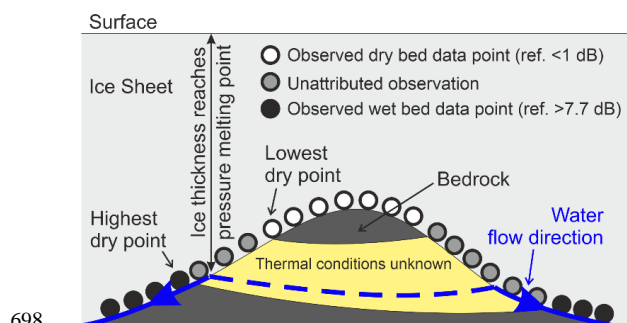
670 Carter et al. (2009) modelled the dielectric loss of radar data through the ice column around Dome C in East
671 Antarctica (Fig. 6) to infer the basal reflectivity and verify the presence of subglacial water. Because the
672 temperature profile of the ice sheet is one parameter affecting dielectric loss, this approach required inference of
673 the basal heat flow from temperature-depth modelling over the last 254 ka. The Shapiro and Ritzwoller (2004)
674 GHF model was used initially (see section “4.2. Seismic estimates”), but when the calculated vertical ice velocity
675 (m_w) at the bed exceeded the initial melt rate (m_T), the GHF was modified until m_T and m_w were equal. This
676 approach identified localised high GHF anomalies, but (excepting these anomalies) they calculated that 66 % of
677 the study area was either at or near the pressure melting point (anywhere that ice is thicker than 3500 m) without
678 invoking enhanced GHF.

679 Schroeder et al. (2014) modelled the spatial distribution of melt beneath the ice sheet in the Thwaites Glacier
680 catchment (Fig. 6) by mapping the relative bed echo strength of radar data in the region and modelling the water
681 routing required to match these observations by routing alone (without heterogeneous basal melting). These
682 routing models were based on the radar-derived ice thickness and surface slope. The 50 selected routing models
683 were used to model the relative melt required to reproduce the observed echo strengths of each routing model.
684 This relative melt model was in turn scaled to match the total melt water produced in an ice sheet model of the
685 Thwaites Glacier incorporating frictional melting, horizontal advection, and an assumed uniform GHF. By
686 subtracting the frictional and advective contributions, the GHF required to produce the remaining melt could be



687 calculated. This approach predicted very high heat flow in this region (114 to $>200 \text{ mW m}^{-2}$), with the highest
688 heat flow focused around observed and inferred subglacial volcanoes.

689 With the aim of determining appropriate sites of low basal melting for old-ice drilling, Passalacqua et al. (2017)
690 also used radar evidence for basal melting and ice sheet modelling to determine GHF around Dome C (Fig. 6).
691 Wet and dry bed conditions were identified from radar data and ten spots were identified on bedrock topographic
692 features marking the critical ice thickness where present basal melting becomes possible. These spots were defined
693 as locations where the upper slopes of the bedrock topography are dry and their lee slopes are wet, with melting
694 initiating between the two when the ice thickness passes the pressure melting point (Fig. 14). Assuming that GHF
695 is locally homogeneous between the two bedrock elevations, heat flow was determined by increasing its value in
696 a 1-D heat model of the local ice thickness until basal melting occurred. These point estimates were interpolated
697 to generate an approximate map of regional heat flow and calculate basal melt rates over the last 400 ka.



698
699 **Fig. 14. Illustration of how the ice thickness exceeding the pressure melting point (PMP) can be identified from radar**
700 **reflectivity data points, indicating the presence or absence of basal water beneath the ice sheet. Once the PMP is**
701 **identified, thermal modelling can estimate the required local GHF. Between the thresholds of radar reflectivities**
702 **representative of wet and dry basal conditions, the thermal conditions are unknown (yellow-shaded region of the**
703 **bedrock). Adapted from Passalacqua et al. (2017).**

704 Liefvering and Pattyn (2013) and Liefvering et al. (2018) used steady state and transient thermodynamic
705 modelling of the East Antarctic Ice Sheet to map the minimum heat flow required to raise the basal temperature
706 above pressure melting point and generate basal melting. Whilst this was executed to identify possible sites for
707 drilling the oldest ice in areas that are unlikely to have undergone basal melting in the last 1.5 Ma and did not
708 produce an estimate of absolute GHF, if this approach were combined with other evidence for basal conditions
709 above the pressure melting point (e.g. combining thermodynamic modelling with subglacial lake locations) points
710 of minimum heat flow could be mapped.

711 5.2. Subglacial lakes

712 If temperatures are sufficient for basal melting, and topography depressions are suitable, subglacial lakes can
713 develop. Subglacial lakes exhibit radio reflectivities 10-20 dB greater than the ice-bedrock boundary, allowing
714 the current identification of 402 lakes beneath the Antarctic ice sheet.



715 Whether basal temperatures are sufficient for basal melting and preservation of subglacial lakes is dependent on
716 ice thickness, the surface temperature and accumulation rate, heat transported through ice advection, heat
717 produced by internal deformation and basal sliding, and the GHF. When subglacial lakes are located near ice
718 divides, heat derived by horizontal advection, basal friction, and internal deformation is assumed to be minimal,
719 and thus the heat required to bring the base of the ice sheet above the pressure melting point is a product of ice
720 thickness and GHF. Thus, when subglacial lakes are located near ice divides and the accumulation rate is known
721 (high accumulation rates cool the ice mass), point estimates of *minimum* GHF can be calculated from one-
722 dimensional thermal models of the ice sheet temperature profile, but an assumption that water was derived locally
723 and not routed from elsewhere must also be considered as lakes can only form in topographic depressions. The
724 absence of a lake or basal water does not imply the bed is frozen if the water can drain away (Pattyn, 2010; Siegert
725 and Dowdeswell, 1996).

726 5.3. Englacial stratigraphy

727 Jordan et al. (2018) identified draw down of internal ice sheet layers and increased bed reflectivity from radar data
728 near the South Pole (Fig. 6), indicating enhanced basal melting. Melt rates were calculated using dated radar
729 layers, traced from the Dome C ice-core site, and a depth age model that simulates the draw-down effect of ice
730 from subglacial melt rate. The low ice velocity ($<1.5 \text{ m a}^{-1}$) indicated minimal frictional contribution to basal
731 temperature, and a location at the top of a hydraulic catchment area indicated a low heat contribution from
732 subglacial water. By negating these contributions to heat flow, assuming the basal temperature is at the pressure
733 melting point (and thus could be derived from the ice thickness) and that temporal temperature variations match
734 those of the Dome C ice core, a time-dependent heat equation was applied to the ice sheet to derive the basal GHF
735 required to generate the enhanced melt rates.

736 5.4. Microwave emissivity

737 Englacial temperature profiles have been derived from satellite and airborne passive detection of high frequency
738 L-band microwave radiation ($\sim 1.4 \text{ GHz}$; Macelloni et al., 2019, 2016; Passalacqua et al., 2018); data primarily
739 collected to investigate soil moisture and ocean salinity (Kerr et al., 2010). These wavelengths have very low
740 absorption in ice and low scattering by particles (e.g. grainsize and ice bubbles), providing high penetration depths
741 in dry ice.

742 Macelloni et al. (2019) derived englacial temperature profiles for the Antarctic ice sheet from 2-year averaged
743 vertical-polarised (V) radiation collected at the “Brewster angle” ($57.1^\circ \pm 2.6^\circ$; the angle of incidence at which the
744 radiation is perfectly transmitted through the air-snow interface with no reflection, minimising the influence of
745 surface or shallow sub-surface effects). The corrected intensity (brightness temperature, T_B) correlates with the
746 surface temperature of the ice, but is also affected by the ice sheet thickness (a largely inverse correlation), density
747 profile, and grain size (Macelloni et al., 2016). As such, the ice sheet’s thermal structure at depth could be
748 estimated by comparing the observed T_B and a simulated T_B derived through microwave emissivity modelling,
749 including one-dimensional modelling of the ice sheet’s temperature profile. Included in the assumed values for
750 this modelling are the GHF and the accumulation rate; the sources of greatest uncertainty. This method only
751 applies in areas of slow flowing ice ($<10 \text{ m yr}^{-1}$), and is optimal in areas of very slow flowing ice ($<5 \text{ m yr}^{-1}$) as

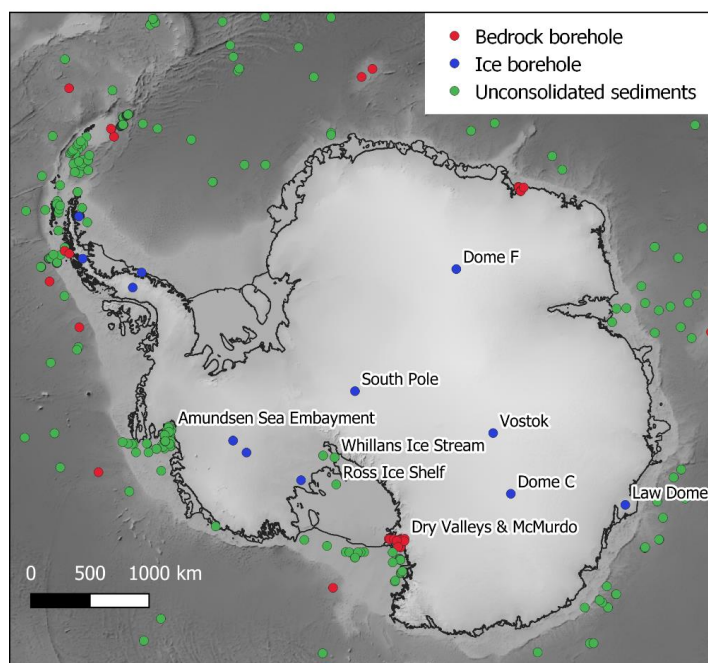


752 this negates heating by horizontal ice advection and deformation-derived heat production. It is also only applicable
753 to areas of thick ice (>1000 m) as the simulations used to model microwave emission do not include bedrock
754 reflections. This is not a limitation for application to Antarctic GHF research, as it is under these conditions that
755 heat flow has the greatest influence on ice sheet dynamics.

756 Comparison of the microwave-derived temperature profile and that simulated by glaciological modelling
757 (Liefvering and Pattyn, 2013) show good agreement in the upper third of the ice sheet, but diverge in their
758 temperature estimates with depth, with the largest uncertainties close to the bedrock. This is largely due to
759 uncertainty in the GHF, but also reflects a decrease in sensitivity of the simulated T_b to the temperature profile
760 below 1000-1500 m (the bottom 1000-1500 m of the ice sheet contributes <10 % to the total emission). Longer
761 wavelength emissions (0.5 GHz) with greater sensitivity to the deeper temperature profile may provide greater
762 accuracy at depth (Jezek et al., 2014). Deep measurements of the ice sheet's temperature profile are required to
763 validate this method compared to the glaciological models. Although currently limited by its sensitivity to
764 temperature at depth and the accuracy of the assumed parameters (notably accumulation rate), this approach has
765 the potential to constrain basal heat flow through variation of the assumed GHF values used in the emissivity
766 modelling.

767 6. Existing data

768 Although subglacial borehole-derived estimates of terrestrial GHF are lacking in Antarctica, estimates have been
769 made from probes into marine sediments and boreholes into exposed bedrock. We have compiled 433 of these
770 point estimates (Fig. 15; data available in the Supplementary Material and from
771 <https://github.com/RicardaDziadek/Antarctic-GHF-DB>). However, the compiled data originates from multiple
772 methods, and is variable in its accuracy and limitations. We do not include values for marine measurements
773 compiled in the database "Global Heat Flow Data – Abbott Compilation". This database is available via
774 GeoMapApp and completely undocumented. The labels may point to cruise reports, but not published data and
775 the data quality remains impossible to evaluate up to this point.



776

777 **Fig. 15. Locations of all compiled point estimates of GHF. Database available in the Supplementary Material and from**
778 <https://github.com/RicardaDziadek/Antarctic-GHF-DB>.

779 6.1. Boreholes into bedrock

780 Terrestrial, borehole-derived measurements of the geothermal gradient are limited to the Dry Valleys and
781 McMurdo Sound region (Fig. 15; Bucher, 1980; Decker, 1974; Decker and Bucher, 1982; Pruss et al., 1974;
782 Talalay and Pyne, 2017), and no subglacial terrestrial borehole measurements have been made into the Antarctic
783 bedrock. However, as discussed in Section 3.1., temperature gradients in bedrock must be taken to a sufficient
784 depth to be representative of upward conduction of the GHF rather than downward conduction of the surface
785 temperature. Whilst the GHF estimates from the Dry Valleys Drilling Project (DVDP, including McMurdo
786 Station) were taken from the 75 to >300 m deep boreholes (Bucher, 1980; Decker and Bucher, 1982; Talalay and
787 Pyne, 2017), the shallow 7.6 m borehole from McMurdo Station produces a much higher GHF estimate (164 mW
788 m⁻², Risk and Hochstein, 1974). This shallow measurement should thus be neglected in preference for the 66 mW
789 m⁻² value from the 260 m deep DVDP borehole (Decker and Bucher, 1982).

790 Boreholes into submarine bedrock have been drilled and temperature gradients measured beneath the McMurdo
791 Sound, Amundsen Sea Embayment, and Ross Ice Shelf (Fig. 15; Bückler et al., 2001; Decker et al., 1975; Gohl et
792 al., 2019; McKay et al., 2018; Morin et al., 2010).

793 The US Rapid Access Ice Drill project (RAID) aims to achieve the first subglacial, borehole-derived thermal
794 measurements of bedrock following drilling of the overlying ice sheet and coring of ≥ 25 m of bedrock (Goode
795 and Severinghaus, 2016).



796 **6.2. Ice boreholes**

797 GHF estimates from ice boreholes are better distributed across the Antarctic continent than terrestrial bedrock
798 boreholes (Fig. 15). However, not all ice boreholes drilled have been sufficiently deep or in appropriate sites for
799 GHF estimation (i.e. the ice sheet needs to be stationary and frozen to the bed). This limits the available GHF
800 estimates to Vostok (Salamat et al., 1998), Dome Fuji (Hondoh et al., 2002), Law Dome (Dahl-Jensen et al.,
801 1999), South Pole (Price et al., 2002), Marie Byrd Land (Clow et al., 2012; Engelhardt, 2004; Gow et al., 1968),
802 and the Antarctic Peninsula (Mulvaney et al., 2012; Nicholls and Paren, 1993; Zagorodnov et al., 2012) (Fig. 15).

803 **6.3. Marine and onshore unconsolidated sediments**

804 The most abundant resource of heat flow estimates from measured temperature profiles around Antarctica comes
805 from unconsolidated marine sediments (Fig. 15). However, the data distribution is sparse and heterogeneous, and
806 whilst some regions are well sampled (e.g. the Amundsen Sea embayment; Dziadek et al., 2019, 2017), other
807 regions (e.g. the Weddell Sea) remain poorly constrained (Fig. 15). In addition to the open water measurements,
808 two shallow probes (deepest sensors at 1.4 and 0.8 m below the upper sediment surface) have measured the
809 temperature gradient in subglacial sediments below the Whillans Ice Stream (Begeman et al., 2017; Fisher et al.,
810 2015; see section 3.3.). Two temperature gradients have also been measured beneath the Ross Ice Shelf (Foster,
811 1978; Morin et al., 2010), but otherwise heat flow beneath the Antarctic ice shelves remains poorly constrained
812 regions.

813 As discussed in Section 3.3, when using these estimates it is important to consider whether the shallow (<~5 m)
814 temperature gradient recorded by the probe is representative of the deeper GHF, or will have been perturbed by
815 temperature variation in the overlying ice sheet or water column (e.g. Dziadek et al., 2019). Consequently, the
816 water depth, the temperature profile of the water column, and possible sources of long-term temperature variation
817 (e.g. variations in deep water circulation and temperature) should be considered when selecting appropriate point
818 estimates. Similarly, whilst the shallow temperature gradients measured from Subglacial Lake Whillans (Fisher
819 et al., 2015), and the Whillans Ice Stream grounding zone (Begeman et al., 2017) are presented as subglacial direct
820 measurements of Antarctic GHF, by the nature of their location within an ice stream they are not in a thermal
821 steady state, and the temperature profile will have been affected by long term variation from heat advection and
822 shear heating. These are effects that cannot be evaluated from their very shallow temperature gradient (0.8 and
823 1.4 m deep), and accordingly these estimates should be used with caution.

824 **7. Current challenges and future research directions**

825 The collated existing data and methodologies presented above highlight our current limitations in determining the
826 subglacial GHF of Antarctica and allow discussion of future research.

827 **7.1. Borehole and probe-derived estimates**

828 The fundamental limitation for GHF estimation in Antarctica is the lack of borehole-derived estimates from
829 beneath the Antarctic ice sheet. Without these independent, discrete validation points, the more extensive regional
830 estimates cannot be accurately evaluated. Therefore, the most promising future development will be the ≥ 25 m
831 deep bedrock borehole measurements of the Rapid Access Ice Drill project (RAID; Goodge and Severinghaus,

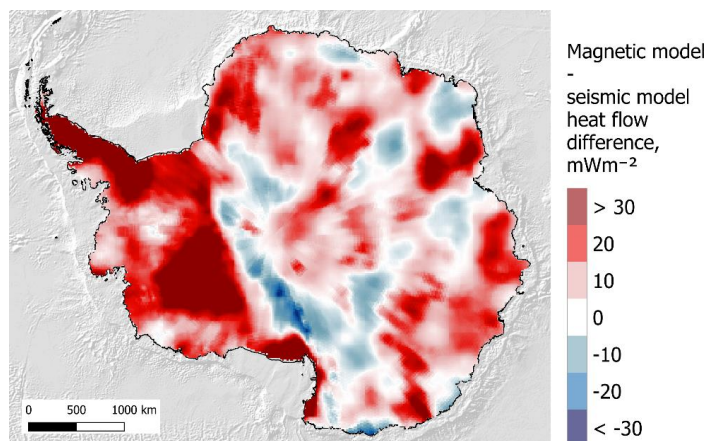


832 2016). However, (as noted above) local temperature gradients may not be representative of the regional heat flow,
833 as local geology, hydrothermal circulation, and topography can result in localised GHF variability. In response,
834 multiple boreholes are required to categorise the regional variation, and topographic effects must be considered
835 and accounted for.

836 It is also a necessity that thermal modelling of the bedrock temperature profile for the RAID target sites is executed
837 prior to drilling to constrain the penetration depth of low-frequency time variation of temperature. Whilst the
838 RAID target bedrock borehole depth of ≥ 25 m is much shallower than the >100 m borehole depth achieved for
839 exposed bedrock (Section 3.1.), the overlying ice sheet insulates the bedrock temperature profile from short
840 duration surface temperature variability (temperature variation penetration depth is dependent on the frequency
841 of the variation and thermal diffusivity of the material; Carslaw and Jaeger, 1959). However, as is considered for
842 GHF estimates from ice boreholes (Section 3.2.), low-frequency variation in surface temperatures, heat advection,
843 and shear heating will all affect the subglacial temperature profile. Consequently, low-frequency temperature
844 variation must be corrected for, and boreholes are best drilled where the ice is stationary and frozen to the bed (as
845 is applied to ice borehole selection for GHF estimation). By drilling in such sites where glaciological approaches
846 are most effective for GHF estimation, the RAID data will allow validation of GHF estimates for the various
847 englacial temperature methods applied to stationary ice at ice divides (Section 5.). These methods include borehole
848 temperature profiles, subglacial lakes, ice sheet models, and microwave emissivity. It is thus important that the
849 englacial temperature profile is measured in addition to the bedrock temperature gradient.

850 Beyond bedrock drilling there is lot to be gained from further ice borehole drilling. Firstly, existing data must be
851 evaluated to ensure the methodologies of GHF modelling from borehole temperature profiles are consistent and
852 accurate. This is particularly true for the Dome C borehole, for which the previously published 49.0 mW m^{-2} value
853 (de Mendoza et al., 2016) has been retracted. Future ice boreholes into stationary ice frozen to the bed has the
854 potential to supplement the existing borehole and probe-derived GHF estimates, particularly if the proposed
855 methodology for shallow boreholes can be validated (600 m depth, or the upper 20% of the ice column; Section
856 3.2.).

857 7.2. Geophysical GHF estimates



858



859 **Fig. 16. Difference in heat flow values between the most recent magnetic (Martos et al., 2017) and seismic (An et al.,**
860 **2015b) heat flow models.**

861 Whilst only geophysical methods have provided continental-scale GHF estimates, their values and distribution
862 vary greatly (Fig. 5 and Fig. 16). Uncertainties of $<10 \text{ mW m}^{-2}$ for the majority of Antarctica were presented for
863 the Curie Depth GHF model of Martos et al. (2017). However, not only are the modelled values greatly different
864 from those derived by seismic modelling (An et al., 2015b), the calculated Curie depth is deeper than the
865 seismically- or gravitationally-derived Moho depth for large areas of the continent (Fig. 10). Whilst this can occur
866 where metallic phases are present in cratonic mantle (Ferré et al., 2013; Section 4.1.), this cannot explain the full
867 distribution, nor are these occurrences likely to be this extensive. Without being critical of the model itself, it is
868 reasonable to dispute the accuracy of the calculated uncertainties, and suggest that whilst their calculation from
869 the geophysical data may be logical, there may be a geological contribution to uncertainty (e.g. lithological
870 variation in the lithosphere) that is not being considered. As GHF models are utilised by researchers in different
871 fields to those publishing the models, they cannot be independently evaluated by the user, and so accuracy in
872 published uncertainty values is arguably more important than the accuracy of the model itself. We recommend
873 that future research (including geophysical, geological, glaciological, and borehole and probe-derived estimates)
874 is careful in its presentation of uncertainty.

875 The largest limitations to existing geophysical-derived GHF models are uncertainties in the structure,
876 composition, heat production, and thermophysical properties of the unexposed crust, lithosphere, and underlying
877 mantle. All current continental models assume the lithosphere to be laterally homogenous in its composition and
878 thermophysical properties, and although seismic GHF models (e.g. An et al., 2015b) incorporate variable mantle
879 temperatures, its composition is assumed to be homogenous. Geophysical GHF models assume that lithospheric
880 heat production is focussed in the upper crust, and is orders of magnitude greater than the deeper heat production
881 of the middle and lower crust and the mantle. These models assume that lithospheric heat production either
882 exponentially decreases with depth (e.g. the Curie depth models of Fox Maule et al., 2005, and Martos et al.,
883 2017) or is concentrated within a laterally homogenous layer of variable depth and constant heat production (e.g.
884 the seismic model of An et al., 2015a, and the thermal-isostatic model for Australia of Hasterok and Gard, 2016).
885 However, although the lower crust is enriched in mafic rocks (iron-rich rocks of high crystallisation temperature,
886 e.g. basalt) of low heat production, deep boreholes and crustal sections have shown that whilst there is a correlation
887 between heat production and lithology in the upper crust, there is no such correlation with depth or metamorphic
888 grade (Section Section 4.6.3.). Similarly, the assumption of laterally homogenous heat production has been shown
889 to be unreasonable for estimation of Antarctica's GHF, which (like all continents) has a laterally variable geology
890 and associated concentration of HPEs (Burton-Johnson et al., 2017; Carson et al., 2014). The exponential decrease
891 model of crustal heat production should thus be rejected, and attempts should be made to derive the depth and
892 structure of crustal heat production.

893 The most promising approach to address the challenge of uncertainty in the contribution to GHF from the
894 unexposed crust and deeper lithosphere is the derivation of a three-dimensional lithospheric structure model for
895 Antarctica. This approach uses geophysical modelling integrating seismic, magnetic, and thermal-isostatic
896 evidence, and integrating into the modelling the heat production, conductivity, and petrophysical properties of
897 exposed lithologies and deeper crustal xenoliths or crustal sections. A similar model was developed for Norway



898 (Ebbing et al., 2006; Olesen et al., 2007), and an Antarctic model would build upon recent 2D and 3D
899 geophysically-derived models (Leat et al., 2018; Pappa et al., 2019b, 2019a). Beneath the Antarctic ice sheet,
900 where the surface geology is unknown, the lithologies and probable heat production is best constrained by
901 determining the probable heat production of each drainage basin based on its detrital clasts (e.g. Goodge, 2018).

902 The assumption of a homogenous mantle composition beneath East Antarctica is challenged by discrepancies
903 between the Moho depth models derived by gravity and isostatic modelling (Pappa et al., 2019b, 2019a), as this
904 indicates variable lithospheric mantle densities, or deeper mantle effects on topography. A review of the available
905 mantle xenoliths and mantle-derived basalt chemistry may be able to constrain the composition of the mantle
906 beneath Antarctica, and thermal-isostatic modelling may be able to identify these regions of anomalous mantle
907 anomalies (as in the Australian study of Hasterok and Gard, 2016). If the seismic data for Antarctica is sufficient
908 to determine crustal density, such a thermal isostatic model would provide an additional independent method to
909 determine the depth of the upper crustal heat producing layer (Hasterok and Chapman, 2011) and evaluate the
910 other GHF models.

911 Finally, it is important to compare Antarctica with its conjugate margins (e.g. Pollett et al., 2019), where GHF and
912 crustal structure are better constrained. This provides constraints on the GHF along the margins of East Antarctica,
913 as well as informing on the geology beneath the ice sheet.

914 7.3. Glaciological GHF estimates

915 Englacial temperatures are more sensitive to GHF in areas of the interior of Antarctica where basal sliding is
916 negligible (Section 2.1). Out of all the methods discussed to derive GHF in the Antarctic interior, the most
917 promising method is to derive GHF from englacial temperatures obtained from microwave emission (Section 5.4.)
918 at a longer wavelength (0.5 GHz) than the currently available (~1.4 GHz). The increase in wavelength will reduce
919 the uncertainty in englacial temperatures below 1000-1500 m (Jezek et al., 2014). By improving the estimations
920 of englacial temperature near the bed, this will reduce the role of ice flow modelling required to extrapolate
921 temperature from the partial-depth data. Potentially, if near-the-bed englacial temperatures are known with
922 sufficient precision, GHF could be derived as from borehole thermometry (Section 3.2). However, this method
923 requires the acquisition of currently unavailable satellite-derived data as, despite the potential of this method, the
924 2018 Cryorad proposal submitted to ESA (Macelloni et al., 2018) was unsuccessful.

925 Existing glaciological data, like subglacial water distribution or dated englacial layers, has been successfully used
926 in estimating heat flow in regions of thick, slow flowing ice near ice divides, where advection and shear heating
927 are minimised. To extend these regional studies to continental scale, both data and models have to be improved.
928 A significant challenge for radar-derived subglacial water distribution is our ability to discriminate between water
929 at the bed versus contrasts in the geometric properties of ice sheet and bed (Schroeder et al., 2014). However the
930 improvement in radar techniques and the combination with seismic surveys and direct access observations, is our
931 best chance to improve our observations of subglacial hydrology (Ashmore and Bingham, 2014).

932 The inventory of subglacial lakes (Wright and Siegert, 2012) is a better constrained and expanding dataset.
933 Subglacial lakes can be detected also using satellite surface altimetry (Fricker et al., 2007), providing a way to
934 expand the coverage and to confirm dubious cases. However, as noted in Section 5.1., topography must be



935 considered when using evidence for subglacial lakes as they can only develop in topographic depressions, and the
936 absence of basal water does not imply the bed is frozen if water can drain away.

937 Subglacial melting can also be detected in englacial stratigraphy (Section 5.3) but the required radar product
938 (internal radar reflective horizons) is not often available. “AntArchitecture” is a SCAR (Scientific Committee on
939 Antarctic Research) Action Group bringing together key datasets on Antarctic internal layering from the principal
940 institutions and scientists who have been responsible for acquiring, processing and storing them over the last four
941 decades (AntArchitecture Action Group, 2017). As the coverage of Antarctic internal layers becomes widely
942 available, its application to infer GHF will increase in popularity.

943 Finally, and for any of the glaciological methods described above, the glaciological models used to infer GHF
944 have to be improved. The current thermal models used to infer GHF can be classified in two larger groups: 1) 1D
945 time-dependent high-complexity models, and 2) 2D/3D steady-state low-complexity models. The first category is
946 generally used near ice domes or ridges, with low horizontal flow, and where horizontal heat advection can be
947 neglected (e.g., Passalacqua, 2017). The latter are used across the whole continent (e.g., Liefferinge, 2018), but
948 ignore the changes in temperature between glacial and interglacial periods despite their strong effect on englacial
949 temperatures (Ritz, 1989). The challenge is to develop thermal models with the required level of complexity at a
950 continental scale, accommodating the main physical processes. This remains a technical challenge.

951 **8. Conclusions**

952 We present state-of-the-art data and models to estimate geothermal heat flow in Antarctica and highlight the need
953 for a detailed continental map. We also discuss current challenges and future directions.

954 With multiple methodologies and models for Antarctic GHF currently published, the most promising future
955 direction is borehole-derived estimation of GHF beneath the Antarctic ice sheet from RAID bedrock drilling and
956 englacial temperatures from ice boreholes. Ideally, the latter approach will be validated by the former to support
957 expansion of the dataset from shallow boreholes (potentially only 600 m deep, or 20 % of the total ice sheet
958 thickness).

959 The ice sheet is most sensitive to variation in GHF within the interior of Antarctica, where heat production from
960 slide at the base of the ice sheet is negligible. However, it is in this region that GHF is hardest to constrain by
961 geophysical estimates because of the scarcity of local GHF estimates from down-hole measured temperature
962 gradients, geological data, and insight from conjugate margins. It is thus in the interior of Antarctica where
963 glaciological approaches are the most applicable. Out of the methods presented, the determination of englacial
964 temperatures from long-wavelength microwave emissivity is the most promising, but this data is not currently
965 available.

966 We highlight the potential of regional estimates of GHF from subglacial meltwater inventories. Aside from the
967 ever expanding inventory of subglacial lakes we encourage initiatives like “AntAntarctica” that will make radar
968 products widely available. Also, we discuss future requirements of thermal models (either 1D or those lacking
969 glacial-interglacial variability) to expand the methods beyond domes in the interior of Antarctica.



970 Geophysical methods remain the most attractive approach to estimate GHF because they are independent of ice
971 flow. However, they vary greatly in their estimated magnitude and distribution of GHF. The greatest uncertainty
972 in all the geophysical models is uncertainty in the composition and structure of the lithosphere and mantle. We
973 recommend ceasing to use the exponential decrease model of crustal heat production. Instead, we suggest using
974 geological and geophysical approaches to model the thickness, structure and composition of the crust. We also
975 recommend the application of a thermal-isostatic approach to provide an independent estimate, and highlight
976 regions of anomalous isostatic elevation and probable mantle heterogeneities.

977 Finally, the greatest challenge for Antarctic GHF estimation is the necessity for multidisciplinary science.
978 Hopefully, this paper provides a first step in communicating the approaches and limitations of the different fields
979 across the GHF community. We sincerely recommend the continuation and enhancement of the international
980 collaborations within SCAR, building on the work of the GHF sub-group of the SERCE research programme
981 (Solid Earth Response and influence on Cryospheric Evolution), and encourage and appreciate SCAR's
982 continuing support in this field of research.

983 **9. Acknowledgements**

984 A. Burton-Johnson and C. Martin were funded by the Natural Environment Research Council as part of the British
985 Antarctic Survey Polar Science for Planet Earth programme. R. Dziadek was supported by the Deutsche
986 Forschungsgemeinschaft (DFG) in the framework of the Priority Program 1158 “Antarctic research with
987 comparative investigations in Arctic ice areas” by grant GO 724/14-1. Additional funds were contributed by the
988 AWI Research Program PACES-II Workpackage 3.2. This research is a contribution to the SCAR SERCE
989 programme, and we thank the discussions and support of this group from the TACTical 2018 (Hobart, Australia),
990 POLAR 2018 (Davos, Switzerland), and ISAES 2019 (Incheon, Korea) meetings. We particularly thank
991 Jacqueline Halpin (IMAS) for her comments on the manuscript and her in work promoting and developing the
992 Antarctic GHF community.

993 **10. References**

- 994 About, E., Salem, A. and Mekkawi, M.: Curie depth map for Sinai Peninsula, Egypt deduced from the analysis
995 of magnetic data, *Tectonophysics*, 506(1–4), 46–54, 2011.
- 996 Aitken, A. R. A., Betts, P. G., Young, D. A., Blankenship, D. D., Roberts, J. L. and Siegert, M. J.: The Australo-
997 Antarctic Columbia to Gondwana transition, *Gondwana Research*, 29(1), 136–152, 2016.
- 998 Alessio, K. L., Hand, M., Kelsey, D. E., Williams, M. A., Morrissey, L. J. and Barovich, K.: Conservation of deep
999 crustal heat production, *Geology*, 46(4), 335–338, 2018.
- 1000 Amante, C. and Eakins, B. W.: ETOPO1 Arc-Minute Global Relief Model: Procedures, Data Sources and
1001 Analysis, National Oceanic and Atmospheric Administration Technical Memorandum NESDIS NGDC-24., 2009.
- 1002 An, M., Wiens, D. A., Zhao, Y., Feng, M., Nyblade, A. A., Kanao, M., Li, Y., Maggi, A. and L ev eque, J.-J.: S-
1003 velocity model and inferred Moho topography beneath the Antarctic Plate from Rayleigh waves, *Journal of*
1004 *Geophysical Research: Solid Earth*, 120(1), 359–383, 2015a.
- 1005 An, M., Wiens, D. A., Zhao, Y., Feng, M., Nyblade, A., Kanao, M., Li, Y., Maggi, A. and L ev eque, J.-J.:
1006 Temperature, lithosphere-asthenosphere boundary, and heat flux beneath the Antarctic Plate inferred from seismic
1007 velocities, *Journal of Geophysical Research: Solid Earth*, 120(12), 8720–8742, 2015b.



- 1008 Andrés, J., Marzán, I., Ayarza, P., Martí, D., Palomeras, I., Torné, M., Campbell, S. and Carbonell, R.: Curie point
1009 depth of the Iberian Peninsula and surrounding margins. A thermal and tectonic perspective of its evolution,
1010 *Journal of Geophysical Research: Solid Earth*, 123(3), 2049–2068, 2018.
- 1011 AntArchitecture Action Group: AntArchitecture: Archiving and interrogating Antarctica’s internal structure from
1012 radar sounding. Final Report, University of Edinburgh, UK. [online] Available from:
1013 <https://www.scar.org/library/science-4/geosciences/antarchitecture/5240-antarchitecture-workshop-2017/file>,
1014 2017.
- 1015 Arnaiz-Rodríguez, M. S. and Orihuela, N.: Curie point depth in Venezuela and the Eastern Caribbean,
1016 *Tectonophysics*, 590, 38–51, 2013.
- 1017 Artemieva, I.: *Lithosphere: an interdisciplinary approach*, Cambridge University Press, Cambridge, UK., 2011.
- 1018 Artemieva, I. M. and Mooney, W. D.: Thermal thickness and evolution of Precambrian lithosphere: A global
1019 study, *Journal of Geophysical Research: Solid Earth*, 106(B8), 16387–16414, 2001.
- 1020 Ashmore, D. W. and Bingham, R. G.: Antarctic subglacial hydrology: current knowledge and future challenges,
1021 *Antarctic Science*, 26(6), 758–773, 2014.
- 1022 Bansal, A. R., Gabriel, G., Dimri, V. P. and Krawczyk, C. M.: Estimation of depth to the bottom of magnetic
1023 sources by a modified centroid method for fractal distribution of sources: An application to aeromagnetic data in
1024 Germany, *Geophysics*, 76(3), L11–L22, 2011.
- 1025 Bansal, A. R., Anand, S. P., Rajaram, M., Rao, V. K. and Dimri, V. P.: Depth to the bottom of magnetic sources
1026 (DBMS) from aeromagnetic data of Central India using modified centroid method for fractal distribution of
1027 sources, *Tectonophysics*, 603, 155–161, 2013.
- 1028 Barletta, V. R., Bevis, M., Smith, B. E., Wilson, T., Brown, A., Bordoni, A., Willis, M., Khan, S. A., Rovira-
1029 Navarro, M. and Dalziel, I.: Observed rapid bedrock uplift in Amundsen Sea Embayment promotes ice-sheet
1030 stability, *Science*, 360(6395), 1335–1339, 2018.
- 1031 Baron Fourier, J. B. J.: *Théorie analytique de la chaleur*, Chez Firmin Didot, père et fils, Paris., 1822.
- 1032 Barrett, B. E., Nicholls, K. W., Murray, T., Smith, A. M. and Vaughan, D. G.: Rapid recent warming on Rutford
1033 Ice Stream, West Antarctica, from borehole thermometry, *Geophysical Research Letters*, 36(2) [online] Available
1034 from: <http://onlinelibrary.wiley.com/doi/10.1029/2008GL036369/full> (Accessed 22 March 2017), 2009.
- 1035 Bea, F.: The sources of energy for crustal melting and the geochemistry of heat-producing elements, *Lithos*, 153,
1036 278–291, doi:10.1016/j.lithos.2012.01.017, 2012.
- 1037 Bea, F. and Montero, P.: Behavior of accessory phases and redistribution of Zr, REE, Y, Th, and U during
1038 metamorphism and partial melting of metapelites in the lower crust: an example from the Kinzigite Formation of
1039 Ivrea-Verbanò, NW Italy, *Geochimica et Cosmochimica Acta*, 63(7), 1133–1153, 1999.
- 1040 Beamish, D. and Busby, J.: The Cornubian geothermal province: heat production and flow in SW England:
1041 estimates from boreholes and airborne gamma-ray measurements, *Geothermal Energy*, 4(1), 4, 2016.
- 1042 Beardsmore, G. R. and Cull, J. P.: *Crustal heat flow: a guide to measurement and modelling*, Cambridge
1043 University Press, Cambridge, UK., 2001.
- 1044 Begeman, C. B., Tulaczyk, S. M. and Fisher, A. T.: Spatially variable geothermal heat flux in West Antarctica:
1045 evidence and implications, *Geophysical Research Letters*, 44(19), 9823–9832, 2017.
- 1046 Berg, J. H., Moscati, R. J. and Herz, D. L.: A petrologic geotherm from a continental rift in Antarctica, *Earth and
1047 Planetary Science Letters*, 93(1), 98–108, 1989.



- 1048 Bhattacharyya, B. K. and Leu, L.-K.: Analysis of magnetic anomalies over Yellowstone National Park: mapping
1049 of Curie point isothermal surface for geothermal reconnaissance, *Journal of Geophysical Research*, 80(32), 4461–
1050 4465, 1975.
- 1051 Blakely, R. J.: *Potential theory in gravity and magnetic applications*, Cambridge university press, Cambridge,
1052 UK., 1996.
- 1053 Blakely, R. J., Brocher, T. M. and Wells, R. E.: Subduction-zone magnetic anomalies and implications for
1054 hydrated forearc mantle, *Geology*, 33(6), 445–448, 2005.
- 1055 Boden, D. R.: *Geology and Heat Architecture of the Earth's Interior*, in *Geologic Fundamentals of Geothermal*
1056 *Energy*, Routledge., 2016.
- 1057 Bodorkos, S., Sandiford, M., Minty, B. R. and Blewett, R. S.: A high-resolution, calibrated airborne radiometric
1058 dataset applied to the estimation of crustal heat production in the Archaean northern Pilbara Craton, Western
1059 Australia, *Precambrian Research*, 128(1–2), 57–82, 2004.
- 1060 Bucher, G. J.: *Heat flow and radioactivity studies in the Ross Island-Dry Valley area, Antarctica and their tectonic*
1061 *implications.*, PhD Thesis, University of Wyoming, Wyoming, USA., 1980.
- 1062 Bücker, C., Jarrard, R. D. and Wonik, T.: Downhole temperature, radiogenic heat production, and heat flow from
1063 the CRP-3 drillhole, Victoria Land Basin, Antarctica, *Terra Antarctica*, 8(3), 151–160, 2001.
- 1064 Bullard, E. C.: The disturbance of the temperature gradient in the earth's crust by inequalities of height,
1065 *Geophysical Supplements to the Monthly Notices of the Royal Astronomical Society*, 4(5), 360–362, 1938.
- 1066 Bullard, E. C.: The time taken for a borehole to attain temperature equilibrium, *Monthly Notices of the Royal*
1067 *Astronomical Society, Geophysics Supplement*, 5, 127–130, 1947.
- 1068 Burton-Johnson, A., Halpin, J. A., Whittaker, J. M., Graham, F. S. and Watson, S. J.: A new heat flux model for
1069 the Antarctic Peninsula incorporating spatially variable upper crustal radiogenic heat production, *Geophysical*
1070 *Research Letters*, 44(11), 5436–5446, doi:10.1002/2017GL073596, 2017.
- 1071 Burton-Johnson, A., Dziadek, R. and Shen, W.: Report of the Geothermal Heat Flux Side Meeting at XIII ISAES,
1072 2019, Incheon, Republic of Korea. [online] Available from: <https://www.scar.org/scar-library/search/science-4/research-programmes/serce/5334-ghf-meeting-report-2019/file>, 2019.
- 1074 Carlson, R. W., Pearson, D. G. and James, D. E.: Physical, chemical and chronological characteristics of
1075 continental mantle, *Reviews in Geophysics*, 43, RG1001, doi:10.1029/2004RG000156, 2005.
- 1076 Carslaw, H. S. and Jaeger, J. C.: *Conduction of heat in solids*, Oxford: Clarendon Press, 1959, 2nd ed., 1959.
- 1077 Carson, C. J. and Pittard, M.: *A Reconnaissance Crustal Heat Production Assessment of the Australian Antarctic*
1078 *Territory (AAT)*, Geoscience Australia, Canberra, Australia., 2012.
- 1079 Carson, C. J., McLaren, S., Roberts, J. L., Boger, S. D. and Blankenship, D. D.: Hot rocks in a cold place: high
1080 sub-glacial heat flow in East Antarctica, *Journal of the Geological Society*, 171(1), 9–12, 2014.
- 1081 Carter, S. P., Blankenship, D. D., Young, D. A. and Holt, J. W.: Using radar-sounding data to identify the
1082 distribution and sources of subglacial water: application to Dome C, East Antarctica, *Journal of Glaciology*,
1083 55(194), 1025–1040, 2009.
- 1084 Chen, B., Haeger, C., Kaban, M. K. and Petrunin, A. G.: Variations of the effective elastic thickness reveal tectonic
1085 fragmentation of the Antarctic lithosphere, *Tectonophysics*, 746, 412–424, 2018.
- 1086 Clauser, C., Giese, P., Huenges, E., Kohl, T., Lehmann, H., Rybach, L., Šafanda, J., Wilhelm, H., Windloff, K.
1087 and Zoth, G.: The thermal regime of the crystalline continental crust: implications from the KTB, *Journal of*
1088 *Geophysical Research: Solid Earth*, 102(B8), 18417–18441, 1997.



- 1089 Clow, G. D., Cuffey, K. M. and Waddington, E. D.: High heat-flow beneath the central portion of the West
1090 Antarctic Ice Sheet, in AGU Fall Meeting Abstracts., 2012.
- 1091 Courtney, R. C. and White, R. S.: Anomalous heat flow and geoid across the Cape Verde Rise: evidence for
1092 dynamic support from a thermal plume in the mantle, *Geophysical Journal International*, 87(3), 815–867, 1986.
- 1093 Cuffey, K. M. and Paterson, W. S. B.: *The physics of glaciers*, Academic Press., 2010.
- 1094 Cuffey, K. M., Clow, G. D., Alley, R. B., Stuiver, M., Waddington, E. D. and Saltus, R. W.: Large arctic
1095 temperature change at the Wisconsin-Holocene glacial transition, *Science*, 270(5235), 455–458, 1995.
- 1096 Daczko, N. R., Halpin, J. A., Fitzsimons, I. C. and Whittaker, J. M.: A cryptic Gondwana-forming orogen located
1097 in Antarctica, *Scientific reports*, 8(1), 8371, 2018.
- 1098 Dahl-Jensen, D., Morgan, V. I. and Elcheikh, A.: Monte Carlo inverse modelling of the Law Dome (Antarctica)
1099 temperature profile, *Annals of Glaciology*, 29, 145–150, 1999.
- 1100 Dalby, C. J., Shail, R. K., Batchelor, A., Cotton, L., Gutmanis, J., Rollinson, G. K., Wall, F. and Hickey, J.: Deep
1101 geothermal energy from the Cornubian Batholith: preliminary lithological and heat flow insights from the United
1102 Downs Deep Geothermal Power Project, Plymouth, UK., 2020.
- 1103 Decker, E. R.: Preliminary geothermal studies of the Dry Valley Drilling Project holes at McMurdo Station, Lake
1104 Vanda, Lake Vida, and New Harbor, Antarctica, *Bulletin-Dry Valley Drilling Project (DVDP)*, 4, 22–23, 1974.
- 1105 Decker, E. R. and Bucher, G. J.: Geothermal studies in the Ross Island-Dry Valley region, *Antarct Geosci*, 4, 887–
1106 894, 1982.
- 1107 Decker, E. R., Baker, K. H. and Harris, H.: Geothermal studies in the Dry Valleys and on Ross Island, *Antarctic
1108 Journal*, 10(4), 176, 1975.
- 1109 Dyment, J. and Arkani-Hamed, J.: Equivalent source magnetic dipoles revisited, *Geophysical Research Letters*,
1110 25(11), 2003–2006, 1998.
- 1111 Dziadek, R., Gohl, K., Diehl, A. and Kaul, N.: Geothermal heat flux in the Amundsen Sea sector of West
1112 Antarctica: New insights from temperature measurements, depth to the bottom of the magnetic source estimation,
1113 and thermal modeling, *Geochemistry, Geophysics, Geosystems*, 18(7), 2657–2672, 2017.
- 1114 Dziadek, R., Gohl, K. and Kaul, N.: Elevated geothermal surface heat flow in the Amundsen Sea Embayment,
1115 West Antarctica, *Earth and Planetary Science Letters*, 506, 530–539, 2019.
- 1116 Ebbing, J., Lundin, E., Olesen, O. and Hansen, E. K.: The mid-Norwegian margin: a discussion of crustal
1117 lineaments, mafic intrusions, and remnants of the Caledonian root by 3D density modelling and structural
1118 interpretation, *Journal of the Geological Society*, 163(1), 47–59, 2006.
- 1119 Elbeze, A. C.: On the existence of another source of heat production for the earth and planets, and its connection
1120 with gravitomagnetism, *SpringerPlus*, 2(1), 1–13, doi:10.1186/2193-1801-2-513, 2013.
- 1121 Engelhardt, H.: Ice temperature and high geothermal flux at Siple Dome, West Antarctica, from borehole
1122 measurements, *Journal of Glaciology*, 50(169), 251–256, 2004.
- 1123 Fahnestock, M., Abdalati, W., Joughin, I., Brozena, J. and Gogineni, P.: High geothermal heat flow, basal melt,
1124 and the origin of rapid ice flow in central Greenland, *Science*, 294(5550), 2338–2342, 2001.
- 1125 Ferraccioli, F., Finn, C. A., Jordan, T. A., Bell, R. E., Anderson, L. M. and Damaske, D.: East Antarctic rifting
1126 triggers uplift of the Gamburtsev Mountains, *Nature*, 479(7373), 388–392, 2011.
- 1127 Ferré, E. C., Friedman, S. A., Martín-Hernández, F., Feinberg, J. M., Conder, J. A. and Ionov, D. A.: The
1128 magnetism of mantle xenoliths and potential implications for sub-Moho magnetic sources, *Geophysical Research
1129 Letters*, 40(1), 105–110, 2013.



- 1130 Fisher, A. T. and Harris, R. N.: Using seafloor heat flow as a tracer to map subseafloor fluid flow in the ocean
1131 crust, *Geofluids*, 10(1–2), 142–160, 2010.
- 1132 Fisher, A. T., Mankoff, K. D., Tulaczyk, S. M., Tyler, S. W., Foley, N. and others: High geothermal heat flux
1133 measured below the West Antarctic Ice Sheet, *Science advances*, 1(6), e1500093, 2015.
- 1134 Flowerdew, M. J., Tyrrell, S., Boger, S. D., Fitzsimons, I. C. W., Harley, S. L., Mikhalsky, E. V. and Vaughan,
1135 A. P. M.: Pb isotopic domains from the Indian Ocean sector of Antarctica: implications for past Antarctica–India
1136 connections, *Geological Society, London, Special Publications*, 383(1), 59–72, 2013.
- 1137 Foster, T. D.: Temperature and salinity fields under the Ross Ice Shelf, *Antarctic Journal [of the United States]*,
1138 13, 81–82, 1978.
- 1139 Fox Maule, C., Purucker, M. E., Olsen, N. and Mosegaard, K.: Heat flux anomalies in Antarctica revealed by
1140 satellite magnetic data, *Science*, 309(5733), 464–467, 2005.
- 1141 Fricker, H. A., Scambos, T., Bindshadler, R. and Padman, L.: An active subglacial water system in West
1142 Antarctica mapped from space, *Science*, 315(5818), 1544–1548, 2007.
- 1143 Frost, B. R. and Shive, P. N.: Magnetic mineralogy of the lower continental-crust, *Journal of Geophysical
1144 Research-Solid Earth and Planets*, 91(B6), 6513–6521, 1986.
- 1145 Fudge, T. J., Biyani, S., Clemens-Sewall, D. and Hawley, B.: Constraining geothermal flux at coastal domes of
1146 the Ross Ice Sheet, Antarctica, *Geophysical Research Letters*, 2019.
- 1147 Gard, M., Hasterok, D. and Halpin, J. A.: Global whole-rock geochemical database compilation, *Earth System
1148 Science Data*, 11(4), 1553–1566, doi:<https://doi.org/10.5194/essd-2019-50>, 2019.
- 1149 Godey, S., Deschamps, F., Trampert, J. and Snieder, R.: Thermal and compositional anomalies beneath the North
1150 American continent, *Journal of Geophysical Research: Solid Earth*, 109(B1), 2004.
- 1151 Goelzer, H., Robinson, A., Seroussi, H. and Van De Wal, R. S.: Recent progress in Greenland ice sheet modelling,
1152 *Current climate change reports*, 3(4), 291–302, 2017.
- 1153 Gohl, K., Wellner, J. S., Klaus, A. and Expedition 379 Scientists: Expedition 379 Preliminary Report: Amundsen
1154 Sea West Antarctic Ice Sheet History, *International Ocean Discovery Program, 379*,
1155 doi:<https://doi.org/10.14379/iodp.pr.379.2019>, 2019.
- 1156 Golynsky, A., Chiappini, M., Damaske, D., Ferraccioli, F., Finn, C. A., Ishihara, T., Kim, H. R., Kovacs, L.,
1157 Masolov, V. N., Morris, P. and others: ADMAP—a digital magnetic anomaly map of the Antarctic, in *Antarctica*,
1158 pp. 109–116, Springer., 2006.
- 1159 Goodge, J. W.: Crustal heat production and estimate of terrestrial heat flow in central East Antarctica, with
1160 implications for thermal input to the East Antarctic ice sheet., *Cryosphere*, 12(2), 2018.
- 1161 Goodge, J. W. and Severinghaus, J. P.: Rapid Access Ice Drill: a new tool for exploration of the deep Antarctic
1162 ice sheets and subglacial geology, *Journal of Glaciology*, 62(236), 1049–1064, 2016.
- 1163 Gow, A. J., Ueda, H. T. and Garfield, D. E.: Antarctic ice sheet: preliminary results of first core hole to bedrock,
1164 *Science*, 161(3845), 1011–1013, 1968.
- 1165 Grauch, V. J. S.: Limitations on digital filtering of the DNAG magnetic data set for the conterminous US,
1166 *Geophysics*, 58(9), 1281–1296, 1993.
- 1167 Greve, R. and Hutter, K.: Polythermal three-dimensional modelling of the Greenland ice sheet with varied
1168 geothermal heat flux, *Annals of Glaciology*, 21(1), 8–12, 1995.
- 1169 Guimarães, S. N. P., Hamza, V. M. and Ravat, D.: Curie depths using combined analysis of centroid and matched
1170 filtering methods in inferring thermomagnetic characteristics of Central Brazil, in *13th International Congress of*



- 1171 the Brazilian Geophysical Society & EXPOGEF, Rio de Janeiro, Brazil, 26–29 August 2013, pp. 1853–1858,
1172 Society of Exploration Geophysicists and Brazilian Geophysical Society., 2013.
- 1173 Gutenberg, B.: 6. Temperature and Thermal Processes in the Earth, in *International Geophysics*, vol. 1, edited by
1174 B. Gutenberg, pp. 121–148, Academic Press Inc., New York., 1959.
- 1175 Haggerty, S. E.: Mineralogical constraints on Curie isotherms in deep crustal magnetic anomalies, *Geophysical
1176 Research Letters*, 5(2), 105–108, 1978.
- 1177 Halpin, J. A. and Reading, A. M.: Report on Taking the Temperature of the Antarctic Continent (TACTical)
1178 Workshop 21–23 March 2018, Hobart, Tasmania, Australia, Hobart, Australia., 2018.
- 1179 Halpin, J. A., Whittaker, J. M., Gard, M., Hasterok, D., Burton-Johnson, A., Staal, T., Maritati, A., Reading, A.
1180 M., McLaren, S., Hand, M. and Raimondo, T.: Heterogenous Antarctic crustal heat production, Incheon, Republic
1181 of Korea., 2019.
- 1182 Han, U. and Chapman, D. S.: Thermal isostasy: Elevation change of geologic provinces, *Journal of the Geological
1183 Society of Korea*, 31(2), 106–115, 1995.
- 1184 Hasterok, D. and Chapman, D. S.: Continental thermal isostasy: 1. Methods and sensitivity, *Journal of
1185 Geophysical Research: Solid Earth*, 112(B6), 2007a.
- 1186 Hasterok, D. and Chapman, D. S.: Continental thermal isostasy: 2. Application to North America, *Journal of
1187 Geophysical Research: Solid Earth*, 112(B6), 2007b.
- 1188 Hasterok, D. and Chapman, D. S.: Heat production and geotherms for the continental lithosphere, *Earth and
1189 Planetary Science Letters*, 307(1–2), 59–70, doi:10.1016/j.epsl.2011.04.034, 2011.
- 1190 Hasterok, D. and Gard, M.: Utilizing thermal isostasy to estimate sub-lithospheric heat flow and anomalous crustal
1191 radioactivity, *Earth and Planetary Science Letters*, 450, 197–207, 2016.
- 1192 Hasterok, D. P., Gard, M., Halpin, J. A., Hand, M. P., Pollett, A., McLaren, S., Raimondo, T., Willcocks, S. and
1193 Linke, M.: Constraining Geothermal Heat Flux Beneath Ice Sheets Using Thermal Isostasy, in *AGU Fall Meeting
1194 2019*, AGU., 2019.
- 1195 Hillenbrand, C.-D., Smith, J. A., Hodell, D. A., Greaves, M., Poole, C. R., Kender, S., Williams, M., Andersen,
1196 T. J., Jernas, P. E. and Elderfield, H.: West Antarctic Ice Sheet retreat driven by Holocene warm water incursions,
1197 *Nature*, 547(7661), 43, 2017.
- 1198 Hindmarsh, R. C. and Ritz, C. M.: How deep do you need to drill through ice to measure the geothermal heat
1199 flux?, in *EGU General Assembly Conference Abstracts*, vol. 14, p. 8629., 2012.
- 1200 Hondoh, T., Shoji, H., Watanabe, O., Salamatin, A. N. and Lipenkov, V. Y.: Depth–age and temperature
1201 prediction at Dome Fuji station, East Antarctica, *Annals of Glaciology*, 35, 384–390, 2002.
- 1202 Huang, Y., Chubakov, V., Mantovani, F., Rudnick, R. L. and McDonough, W. F.: A reference Earth model for
1203 the heat-producing elements and associated geoneutrino flux, *Geochemistry, Geophysics, Geosystems*, 14(6),
1204 2003–2029, 2013.
- 1205 Hughes, T.: Modeling ice sheets from the bottom up, *Quaternary Science Reviews*, 28(19–20), 1831–1849, 2009.
- 1206 Hyvönen, E., Turunen, P., Vanhanen, E., Arkimaa, H. and Sutinen, R.: Airborne gamma-ray surveys in Finland,
1207 *Aerogeophysics in Finland*, 2004, 1972.
- 1208 Jaeger, J. C.: Numerical values for the temperature in radial heat flow, *Journal of Mathematics and Physics*, 34(1–
1209 4), 316–321, 1956.
- 1210 Jaeger, J. C.: The effect of the drilling fluid on temperatures measured in bore holes, *Journal of Geophysical
1211 Research*, 66(2), 563–569, 1961.



- 1212 Jaeger, J. C.: Application of the theory of heat conduction to geothermal measurements, *Terrestrial heat flow*, 8,
1213 7–23, 1965.
- 1214 James, D. W.: The thermal diffusivity of ice and water between- 40 and+ 60° C, *Journal of Materials Science*,
1215 3(5), 540–543, 1968.
- 1216 Jezek, K. C., Johnson, J. T., Drinkwater, M. R., Macelloni, G., Tsang, L., Aksoy, M. and Durand, M.: Radiometric
1217 approach for estimating relative changes in intraglacier average temperature, *IEEE Transactions on Geoscience
1218 and Remote Sensing*, 53(1), 134–143, 2014.
- 1219 Jordan, T., Martin, C., Ferraccioli, F., Matsuoka, K., Corr, H., Forsberg, R., Olesen, A. and Siegert, M. J.: Newly
1220 discovered geothermal anomaly at South Pole ice divide; origins and implications, in *Geophysical Research
1221 Abstracts*, vol. 20, p. 15511., 2018.
- 1222 Jordan, T. A., Riley, T. R. and Siddoway, C. S.: The geological history and evolution of West Antarctica, *Nature
1223 Reviews Earth & Environment*, 1, 117–133, 2020.
- 1224 Kawakatsu, H. and Watada, S.: Seismic evidence for deep-water transportation in the mantle, *Science*, 316(5830),
1225 1468–1471, 2007.
- 1226 Kerr, Y. H., Waldteufel, P., Wigneron, J.-P., Delwart, S., Cabot, F., Boutin, J., Escorihuela, M.-J., Font, J., Reul,
1227 N. and Gruhier, C.: The SMOS mission: New tool for monitoring key elements of the global water cycle,
1228 *Proceedings of the IEEE*, 98(5), 666–687, 2010.
- 1229 Kingslake, J., Scherer, R. P., Albrecht, T., Coenen, J., Powell, R. D., Reese, R., Stansell, N. D., Tulaczyk, S.,
1230 Wearing, M. G. and Whitehouse, P. L.: Extensive retreat and re-advance of the West Antarctic Ice Sheet during
1231 the Holocene, *Nature*, 558(7710), 430–434, 2018.
- 1232 Korenaga, J.: Earth’s heat budget: Clairvoyant geoneutrinos, *Nature Geoscience*, 4(9), 581, 2011.
- 1233 Kuchar, J. and Milne, G. A.: The influence of viscosity structure in the lithosphere on predictions from models of
1234 glacial isostatic adjustment, *Journal of Geodynamics*, 86, 1–9, 2015.
- 1235 Lachenbruch, A. H.: Preliminary geothermal model of the Sierra Nevada, *Journal of Geophysical Research*,
1236 73(22), 6977–6989, 1968.
- 1237 Lachenbruch, A. H.: Crustal temperature and heat production: Implications of the linear heat-flow relation, *Journal
1238 of Geophysical Research*, 75(17), 3291–3300, 1970.
- 1239 Lachenbruch, A. H. and Brewer, M. C.: Dissipation of the temperature effect of drilling a well in Arctic Alaska,
1240 *United States Geological Survey Bulletin*, 1083–C, 73–109, 1959.
- 1241 Langel, R. A. and Hinze, W. J.: *The magnetic field of the Earth’s lithosphere: The satellite perspective*, Cambridge
1242 University Press, Cambridge, UK., 1998.
- 1243 Larour, E., Morlighem, M., Seroussi, H., Schiermeier, J. and Rignot, E.: Ice flow sensitivity to geothermal heat
1244 flux of Pine Island Glacier, Antarctica, *Journal of Geophysical Research: Earth Surface*, 117(F4), 2012.
- 1245 Leat, P. T., Jordan, T. A., Flowerdew, M. J., Riley, T. R., Ferraccioli, F. and Whitehouse, M. J.: Jurassic high heat
1246 production granites associated with the Weddell Sea rift system, Antarctica, *Tectonophysics*, 722, 249–264, 2018.
- 1247 Lees, C. H.: On the shapes of the isogeotherms under mountain ranges in radio-active districts, *Proceedings of the
1248 Royal Society of London. Series A, Containing Papers of a Mathematical and Physical Character*, 83(563), 339–
1249 346, 1910.
- 1250 Li, C.-F., Lu, Y. and Wang, J.: A global reference model of Curie-point depths based on EMAG2, *Scientific
1251 reports*, 7, 45129, 2017.



- 1252 Liefvering, B. V. and Pattyn, F.: Using ice-flow models to evaluate potential sites of million year-old ice in
1253 Antarctica, *Climate of the Past*, 9(5), 2335–2345, 2013.
- 1254 Liefvering, B. V., Pattyn, F., Cavitte, M. G., Karlsson, N. B., Young, D. A., Sutter, J. and Eisen, O.: Promising
1255 Oldest Ice sites in East Antarctica based on thermodynamical modelling, *The Cryosphere*, 12(8), 2773–2787,
1256 2018.
- 1257 Llubes, M., Lanseau, C. and Rémy, F.: Relations between basal condition, subglacial hydrological networks and
1258 geothermal flux in Antarctica, *Earth and Planetary Science Letters*, 241(3), 655–662, 2006.
- 1259 Lowrie, W.: *Fundamentals of geophysics*, 2nd ed., Cambridge University Press, Cambridge., 2007.
- 1260 Lucazeau, F.: *Analysis and mapping of an updated terrestrial heat flow dataset*, *Geochemistry, Geophysics,*
1261 *Geosystems*, 2019.
- 1262 Macelloni, G., Leduc-Leballeur, M., Brogioni, M., Ritz, C. and Picard, G.: Analyzing and modeling the SMOS
1263 spatial variations in the East Antarctic Plateau, *Remote sensing of environment*, 180, 193–204, 2016.
- 1264 Macelloni, G., Brogioni, M., Leduc-Leballeur, M., Montomoli, F., Bartsch, A., Mialon, A., Ritz, C., Soteras, J.
1265 C., Stammer, D. and Picard, G.: Cryorad: A Low Frequency Wideband Radiometer Mission for the Study of the
1266 Cryosphere, in *IGARSS 2018-2018 IEEE International Geoscience and Remote Sensing Symposium*, pp. 1998–
1267 2000, IEEE., 2018.
- 1268 Macelloni, G., Leduc-Leballeur, M., Montomoli, F., Brogioni, M., Ritz, C. and Picard, G.: On the retrieval of
1269 internal temperature of Antarctica Ice Sheet by using SMOS observations, *Remote Sensing of Environment*, 233,
1270 111405, 2019.
- 1271 Mareschal, J. C. and Jaupart, C.: Radiogenic heat production, thermal regime and evolution of continental crust,
1272 *Tectonophysics*, 609, 524–534, doi:10.1016/j.tecto.2012.12.001, 2013.
- 1273 Martin, A. P. and van der Wal, W., Eds.: *The Antarctic Mantle*, The Geological Society, London, UK., in prep.
- 1274 Martin, A. P., Cooper, A. F. and Price, R. C.: Increased mantle heat flow with on-going rifting of the West
1275 Antarctic rift system inferred from characterisation of plagioclase peridotite in the shallow Antarctic mantle,
1276 *Lithos*, 190, 173–190, 2014.
- 1277 Martos, Y. M., Catalán, M., Jordan, T. A., Golynsky, A., Golynsky, D., Eagles, G. and Vaughan, D. G.: Heat flux
1278 distribution of Antarctica unveiled, *Geophysical Research Letters*, 44(22), 11–417, 2017.
- 1279 Martos, Y. M., Jordan, T. A., Catalán, M., Jordan, T. M., Bamber, J. L. and Vaughan, D. G.: Geothermal heat flux
1280 reveals the Iceland hotspot track underneath Greenland, *Geophysical Research Letters*, 45(16), 8214–8222, 2018.
- 1281 Maus, S.: Magnetic field model MF7. Retrieved August 28, 2018, from www.geomag.us/models/MF7.html,
1282 2010.
- 1283 Mayhew, M. A.: Inversion of satellite magnetic anomaly data, *Journal of Geophysics*, 45(1), 119–128, 1979.
- 1284 McDonough, W. F. and Sun, S. s.: The composition of the Earth, *Chemical Geology*, 120(3–4), 223–253,
1285 doi:10.1016/0009-2541(94)00140-4, 1995.
- 1286 McKay, R., De Santis, L., Kulhanek, D. K. and Expedition 374 Scientists: International Ocean Discovery Program
1287 Expedition 374 Preliminary Report: Ross Sea West Antarctic Ice Sheet History, International Ocean Discovery
1288 Program, 374, doi:<https://doi.org/10.14379/iodp.pr.374.2018>, 2018.
- 1289 McKenzie, D., Jackson, J. and Priestley, K.: Thermal structure of oceanic and continental lithosphere, *Earth and*
1290 *Planetary Science Letters*, 233(3–4), 337–349, 2005.



- 1291 de Mendoza, I. H., Mareschal, J.-C. and Beltrami, H.: Constraints on glacier flow from temperature-depth profiles
1292 in the ice. Application to EPICA Dome C., *Climate of the Past Discussions*, doi:[https://doi.org/10.5194/cp-2016-](https://doi.org/10.5194/cp-2016-116)
1293 116, 2016.
- 1294 Morgan, J. P., Rüpke, L. H. and White, W. M.: The Current Energetics of Earth's Interior: A Gravitational Energy
1295 Perspective, *Frontiers in Earth Science*, 4(May), 1–28, doi:[10.3389/feart.2016.00046](https://doi.org/10.3389/feart.2016.00046), 2016.
- 1296 Morin, R. H., Williams, T., Henrys, S. A., Magens, D., Niessen, F. and Hansaraj, D.: Heat flow and hydrologic
1297 characteristics at the AND-1B borehole, ANDRILL McMurdo Ice Shelf Project, Antarctica, *Geosphere*, 6(4),
1298 370–378, 2010.
- 1299 Mulder, J. A., Halpin, J. A., Daczko, N. R., Orth, K., Meffre, S., Thompson, J. M. and Morrissey, L. J.: A
1300 Multiproxy provenance approach to uncovering the assembly of East Gondwana in Antarctica, *Geology*, 47(7),
1301 645–649, 2019.
- 1302 Müller, C., Usbeck, R. and Miesner, F.: Temperatures in shallow marine sediments: Influence of thermal
1303 properties, seasonal forcing, and man-made heat sources, *Applied Thermal Engineering*, 108, 20–29, 2016.
- 1304 Mulvaney, R., Abram, N. J., Hindmarsh, R. C., Arrowsmith, C., Fleet, L., Triest, J., Sime, L. C., Alemany, O. and
1305 Foord, S.: Recent Antarctic Peninsula warming relative to Holocene climate and ice-shelf history, *Nature*,
1306 489(7414), 141–144, 2012.
- 1307 Mulvaney, R., Martin, C., Massam, A., Rix, J. and Ritz, C.: Estimating geothermal heat flux from ice sheet
1308 borehole temperature measurements, in *XIII International Symposium on Antarctic Earth Sciences*, Incheon,
1309 Republic of Korea., 2019.
- 1310 Nicholls, K. W. and Paren, J. G.: Extending the Antarctic meteorological record using ice-sheet temperature
1311 profiles, *Journal of climate*, 6(1), 141–150, 1993.
- 1312 Obande, G. E., Lawal, K. M. and Ahmed, L. A.: Spectral analysis of aeromagnetic data for geothermal
1313 investigation of Wikki Warm Spring, north-east Nigeria, *Geothermics*, 50, 85–90, 2014.
- 1314 Okubo, Y., Graf, R. J., Hansen, R. O., Ogawa, K. and Tsu, H.: Curie point depths of the island of Kyushu and
1315 surrounding areas, Japan, *Geophysics*, 50(3), 481–494, 1985.
- 1316 Olesen, O., Balling, N., Barrère, C., Breiner, N., Davidsen, B., Ebbing, J., Elvebakk, H., Gernigon, L., Koziel, J.,
1317 Lutro, O. and others: KONTIKI final report, continental crust and heat generation in 3D, NGU Report, 42, 2007.
- 1318 Pappa, F., Ebbing, J., Ferraccioli, F. and van der Wal, W.: Modeling satellite gravity gradient data to derive
1319 density, temperature, and viscosity structure of the Antarctic lithosphere, *Journal of Geophysical Research: Solid*
1320 *Earth*, 124, 12053–12076, 2019a.
- 1321 Pappa, F., Ebbing, J. and Ferraccioli, F.: Moho Depths of Antarctica: Comparison of Seismic, Gravity, and
1322 Isostatic Results, *Geochemistry, Geophysics, Geosystems*, 20, 2019b.
- 1323 Passalacqua, O., Ritz, C., Parrenin, F., Urbini, S. and Frezzotti, M.: Geothermal flux and basal melt rate in the
1324 Dome C region inferred from radar reflectivity and heat modelling, *The Cryosphere*, 2017.
- 1325 Passalacqua, O., Picard, G., Ritz, C., Leduc-Leballeur, M., Quiquet, A., Larue, F. and Macelloni, G.: Retrieval of
1326 the Absorption Coefficient of L-Band Radiation in Antarctica From SMOS Observations, *Remote Sensing*,
1327 10(12), 1954, 2018.
- 1328 Paterson, W. S. B.: *The physics of glaciers*, Third Edition., Elsevier, Oxford, UK., 1994.
- 1329 Pattyn, F.: Antarctic subglacial conditions inferred from a hybrid ice sheet/ice stream model, *Earth and Planetary*
1330 *Science Letters*, 295(3), 451–461, 2010.
- 1331 Pfender, M. and Villinger, H.: Miniaturized data loggers for deep sea sediment temperature gradient
1332 measurements, *Marine Geology*, 186(3–4), 557–570, 2002.



- 1333 Phaneuf, C. and Mareschal, J.-C.: Estimating concentrations of heat producing elements in the crust near the
1334 Sudbury Neutrino Observatory, Ontario, Canada, *Tectonophysics*, 622, 135–144, 2014.
- 1335 Pittard, M. L., Galton-Fenzi, B. K., Roberts, J. L. and Watson, C. S.: Organization of ice flow by localized regions
1336 of elevated geothermal heat flux, *Geophysical Research Letters*, 43(7), 3342–3350, 2016a.
- 1337 Pittard, M. L., Roberts, J. L., Galton-Fenzi, B. K. and Watson, C. S.: Sensitivity of the Lambert-Amery glacial
1338 system to geothermal heat flux, *Annals of Glaciology*, 57(73), 56–68, 2016b.
- 1339 Pollack, H. N. and Chapman, D. S.: Mantle heat flow, *Earth and Planetary Science Letters*, 34(2), 174–184, 1977.
- 1340 Pollack, H. N., Hurter, S. J. and Johnson, J. R.: Heat flow from the Earth's interior: Analysis of the global data
1341 set, *Reviews of Geophysics*, 31(3), 267–280, doi:10.1029/93RG01249, 1993.
- 1342 Pollard, D., DeConto, R. M. and Nyblade, A. A.: Sensitivity of Cenozoic Antarctic ice sheet variations to
1343 geothermal heat flux, *Global and Planetary Change*, 49(1), 63–74, 2005.
- 1344 Pollett, A., Hasterok, D., Raimondo, T., Halpin, J. A., Hand, M., Bendall, B. and McLaren, S.: Heat flow in
1345 southern Australia and connections with East Antarctica, *Geochemistry, Geophysics, Geosystems*, 2019.
- 1346 Popov, Y. A., Pevzner, S. L., Pimenov, V. P. and Romushkevich, R. A.: New geothermal data from the Kola
1347 superdeep well SG-3, *Tectonophysics*, 306(3–4), 345–366, 1999.
- 1348 Price, P. B., Nagornov, O. V., Bay, R., Chirkin, D., He, Y., Miocinovic, P., Richards, A., Woschnagg, K., Koci,
1349 B. and Zagorodnov, V.: Temperature profile for glacial ice at the South Pole: Implications for life in a nearby
1350 subglacial lake, *Proceedings of the National Academy of Sciences*, 99(12), 7844–7847, 2002.
- 1351 Pruss, E. F., Decker, E. R. and Smithson, S. B.: Preliminary temperature-measurements at DVDP holes 3, 4, 6,
1352 and 8, *Antarctic Journal of the United States*, 9(4), 133–134, 1974.
- 1353 Purucker, M. and Whaler, K.: Crustal magnetism, edited by M. Kono, *Treatise on Geophysics*, 5, 195–237, 2007.
- 1354 Ravat, D., Pignatelli, A., Nicolosi, I. and Chiappini, M.: A study of spectral methods of estimating the depth to
1355 the bottom of magnetic sources from near-surface magnetic anomaly data, *Geophysical Journal International*,
1356 169(2), 421–434, 2007.
- 1357 Rémy, F. and Legresy, B.: Subglacial hydrological networks in Antarctica and their impact on ice flow, *Annals
1358 of Glaciology*, 39, 67–72, 2004.
- 1359 Risk, G. F. and Hochstein, M. P.: Heat flow at arrival heights, Ross Island, Antarctica, *New Zealand Journal of
1360 Geology and Geophysics*, 17(3), 629–644, 1974.
- 1361 Ritz, C.: Time dependent boundary conditions for calculation of temperature fields in ice sheets, in *The Physical
1362 Basis of Ice Sheet Modelling (Proceedings of the Vancouver Symposium, August 1987)*, vol. IAHS Publ. no. 170,
1363 pp. 207–216, Vancouver, Canada., 1987.
- 1364 Ritz, C.: Interpretation of the temperature profile measured at Vostok, East Antarctica, *Annals of glaciology*, 12,
1365 138–144, 1989.
- 1366 Rix, J., Mulvaney, R., Hong, J. and Ashurst, D.: Development of the British Antarctic Survey Rapid Access
1367 Isotope Drill, *Journal of Glaciology*, 65(250), 288–298, 2019.
- 1368 Rogozhina, I., Hagedoorn, J. M., Martinec, Z., Fleming, K., Soucek, O., Greve, R. and Thomas, M.: Effects of
1369 uncertainties in the geothermal heat flux distribution on the Greenland Ice Sheet: An assessment of existing heat
1370 flow models, *Journal of Geophysical Research: Earth Surface*, 117, F02025, doi:doi:10.1029/2011JF002098,
1371 2012.
- 1372 Ross, H. E., Blakely, R. J. and Zoback, M. D.: Testing the use of aeromagnetic data for the determination of Curie
1373 depth in California, *Geophysics*, 71(5), L51–L59, 2006.



- 1374 Roy, R. F., Blackwell, D. D. and Birch, F.: Heat generation of plutonic rocks and continental heat flow provinces,
1375 Earth and Planetary Science Letters, 5, 1–12, 1968.
- 1376 Rudnick, R. and Fountain, D.: Nature and composition of the continental crust: a lower crustal perspective,
1377 Reviews of Geophysics, (95), 267–309, 1995.
- 1378 Rudnick, R. L., McDonough, W. F. and O’Connell, R. J.: Thermal structure, thickness and composition of
1379 continental lithosphere, Chemical Geology, 145(3–4), 395–411, 1998.
- 1380 Rybach, L.: Amount and significance of radioactive heat sources in sediments, Collection colloques seminaires,
1381 44, 311–322, 1986.
- 1382 Salamatin, A. N., Lipenkov, V. Y., Barkov, N. I., Jouzel, J., Petit, J. R. and Raynaud, D.: Ice core age dating and
1383 paleothermometer calibration based on isotope and temperature profiles from deep boreholes at Vostok Station
1384 (East Antarctica), Journal of Geophysical Research: Atmospheres, 103(D8), 8963–8977, 1998.
- 1385 Salem, A., Green, C., Ravat, D., Singh, K. H., East, P., Fairhead, J. D., Mogren, S. and Biegert, E.: Depth to Curie
1386 temperature across the central Red Sea from magnetic data using the de-fractal method, Tectonophysics, 624, 75–
1387 86, 2014.
- 1388 Sandiford, M. and Hand, M.: Controls on the locus of intraplate deformation in central Australia, Earth and
1389 Planetary Science Letters, 162(1–4), 97–110, 1998.
- 1390 Sandiford, M. and McLaren, S.: Tectonic feedback and the ordering of heat producing elements within the
1391 continental lithosphere, Earth and Planetary Science Letters, 204(1), 133–150, 2002.
- 1392 Schroeder, D. M., Blankenship, D. D., Young, D. A. and Quartini, E.: Evidence for elevated and spatially variable
1393 geothermal flux beneath the West Antarctic Ice Sheet, Proceedings of the National Academy of Sciences, 111(25),
1394 9070–9072, 2014.
- 1395 Sclater, J., Jaupart, C. and Galson, D.: The heat flow through oceanic and continental crust and the heat loss of
1396 the Earth, Reviews of Geophysics, 18(1), 269–311, 1980.
- 1397 Shapiro, N. M. and Ritzwoller, M. H.: Monte-Carlo inversion for a global shear-velocity model of the crust and
1398 upper mantle, Geophysical Journal International, 151(1), 88–105, 2002.
- 1399 Shapiro, N. M. and Ritzwoller, M. H.: Inferring surface heat flux distributions guided by a global seismic model:
1400 particular application to Antarctica, Earth and Planetary Science Letters, 223(1), 213–224, 2004.
- 1401 Siegert, M. J.: Antarctic subglacial lakes, Earth-Science Reviews, 50(1), 29–50, 2000.
- 1402 Siegert, M. J. and Dowdeswell, J. A.: Spatial variations in heat at the base of the Antarctic ice sheet from analysis
1403 of the thermal regime above subglacial lakes, Journal of Glaciology, 42(142), 501–509, 1996.
- 1404 Slagstad, T.: Radiogenic heat production of Archaean to Permian geological provinces in Norway., Norwegian
1405 Journal of Geology/Norsk Geologisk Forening, 88(3), 2008.
- 1406 Spector, A. and Grant, F. S.: Statistical models for interpreting aeromagnetic data, Geophysics, 35(2), 293–302,
1407 1970.
- 1408 Stein, C. A. and Stein, S.: A model for the global variation in oceanic depth and heat flow with lithospheric age,
1409 Nature, 359(6391), 123, 1992.
- 1410 Stein, C. A. and Stein, S.: Mantle plumes: heat-flow near Iceland, Astronomy & Geophysics, 44(1), 1–8, 2003.
- 1411 Swanberg, C. A.: Vertical distribution of heat generation in the Idaho batholith, Journal of Geophysical Research,
1412 77(14), 2508–2513, 1972.



- 1413 Talalay, P. G. and Pyne, A. R.: Geological drilling in McMurdo Dry Valleys and McMurdo Sound, Antarctica:
1414 Historical development, *Cold Regions Science and Technology*, 141, 131–162, 2017.
- 1415 Tanaka, A., Okubo, Y. and Matsubayashi, O.: Curie point depth based on spectrum analysis of the magnetic
1416 anomaly data in East and Southeast Asia, *Tectonophysics*, 306(3–4), 461–470, 1999.
- 1417 Taylor, S. R. and McLennan, S. M.: The continental crust: its composition and evolution, [online] Available from:
1418 <http://www.osti.gov/scitech/biblio/6582885> (Accessed 7 March 2017), 1985.
- 1419 Trifonova, P., Zhelev, Z., Petrova, T. and Bojadgieva, K.: Curie point depths of Bulgarian territory inferred from
1420 geomagnetic observations and its correlation with regional thermal structure and seismicity, *Tectonophysics*,
1421 473(3–4), 362–374, 2009.
- 1422 Turcotte, D. L. and Schubert, G.: *Geodynamics*, Cambridge University Press, Cambridge, UK., 2014.
- 1423 Veikkolainen, T. and Kukkonen, I. T.: Highly varying radiogenic heat production in Finland, Fennoscandian
1424 Shield, *Tectonophysics*, 750, 93–116, 2019.
- 1425 Vieli, G.-M. L., Martin, C., Hindmarsh, R. C. A. and Lüthi, M. P.: Basal freeze-on generates complex ice-sheet
1426 stratigraphy, *Nature communications*, 9(1), 1–13, 2018.
- 1427 Vitorello, I. and Pollack, H. N.: On the variation of continental heat flow with age and the thermal evolution of
1428 continents, *Journal of Geophysical Research: Solid Earth*, 85(B2), 983–995, 1980.
- 1429 Vosteen, H.-D. and Schellschmidt, R.: Influence of temperature on thermal conductivity, thermal capacity and
1430 thermal diffusivity for different types of rock, *Physics and Chemistry of the Earth, Parts A/B/C*, 28(9–11), 499–
1431 509, 2003.
- 1432 van der Wal, W., Barnhoorn, A., Stocchi, P., Gradmann, S., Wu, P., Drury, M. and Vermeersen, B.: Glacial
1433 isostatic adjustment model with composite 3-D Earth rheology for Fennoscandia, *Geophysical Journal
1434 International*, 194(1), 61–77, 2013.
- 1435 van der Wal, W., Whitehouse, P. L. and Schrama, E. J.: Effect of GIA models with 3D composite mantle viscosity
1436 on GRACE mass balance estimates for Antarctica, *Earth and Planetary Science Letters*, 414, 134–143, 2015.
- 1437 Wangen, M.: *Physical principles of sedimentary basin analysis*, Cambridge University Press, Cambridge, UK.,
1438 2010.
- 1439 Wasilewski, P. J. and Mayhew, M. A.: The Moho as a magnetic boundary revisited, *Geophysical Research Letters*,
1440 19(22), 2259–2262, 1992.
- 1441 Winsborrow, M. C., Clark, C. D. and Stokes, C. R.: What controls the location of ice streams?, *Earth-Science
1442 Reviews*, 103(1), 45–59, 2010.
- 1443 Wright, A. and Siegert, M.: A fourth inventory of Antarctic subglacial lakes, *Antarctic Science*, 24(6), 659–664,
1444 2012.
- 1445 Zagorodnov, V., Nagornov, O., Scambos, T. A., Muto, A., Mosley-Thompson, E., Pettit, E. C. and Tyuffin, S.:
1446 Borehole temperatures reveal details of 20th century warming at Bruce Plateau, Antarctic Peninsula, *The
1447 Cryosphere*, 6(3), 675–686, 2012.
- 1448